EFFECTS OF SEVERAL DEFECTS ON THE ELECTROLUMINESCENCE OF 4H-SIC

BY

TINGWEI ZHANG, B.Eng.

A THESIS

SUBMITTED TO THE DEPARTMENT OF MATERIALS SCIENCE AND ENGINEERING AND THE SCHOOL OF GRADUATE STUDIES OF MCMASTER UNIVERSITY

IN PARTIAL FULFILMENT OF THE REQUIREMENTS FOR THE DEGREE OF

MASTER OF APPLIED SCIENCE

Master of Applied Science (2022) McMaster University

Department of Materials Science and Engineering Hamilton, Ontario, Canada

TITLE: Effects Of Several Defects On The Electroluminescence Of 4H-SiC

AUTHOR: Tingwei Zhang

B.Eng. (Materials Science and Engineering),

McMaster University, Hamilton, Canada

SUPERVISOR: Professor Adrian Kitai

NUMBER OF PAGES: xiii, 77

Abstract

Silicon carbide is known for its potential in high power, high radiation and high temperature applications. It is also one of the first materials observed with phenomenon of electroluminescence. Depending on the mechanism of recombination, carriers inside silicon carbide recombine and release photons at different wavelengths. As one of the third-generation semiconductors, many studies focus on the effects of defects on silicon carbide device stability and performance. Especially for defects like stacking faults, which can be generated either during fabrication or induced by current under forward bias, can cause severe device degradation and limits the use of silicon carbide. By testing electroluminescence of silicon carbide, one can analyses the recombination event and identify the defects that trapped carriers, as each recombination mechanism would be shown as a unique emission peak on the sample EL spectra. In addition to the as-grown and recombination-induced defects, the changes of spectrum due to stress and chemical etching indicate the influence of external factors to the defects that are either existed prior to the external forces or that were induced during the testing. Such analysis could be helpful to understand the defect generation mechanism, reduce the density of the defects and to create innovative ideas for future applications. A general introduction to silicon carbide will be given in Chapter 1 with some detailed description of silicon carbide defect generation and

characterization mechanisms in Chapter 2. In Chapters 3 and 4, the focus is to analyse the external effects to the spectrum of 4H silicon carbide, like chemical etching and mechanical stress. Before giving the conclusion in Chapter 6, Chapter 5 will be focusing on analysing the effect of external forces on the silicon carbide with stacking faults existed prior to the testing.

To my family

Acknowledgements

During my graduate study, I would like to express my sincere gratitude to all who supported me:

Thank you for your kind help for me to be able to complete these tasks.

Professor Kitai, for your guidance and wisdom through my graduate study.

Professor Rubel, thank you for all your academic advice and being my committee member.

Doris, thank you for all your kindness and help on accessing the equipment.

Doug and Xiaogang, thank you for all the support with equipment setting.

Gary, for all your cheer that helped me through difficulties.

My family, for all your trust and understanding

Without you, I would not be able to achieve anything.

Contents

List of Figures

List of Tables

Abbreviations and Notations

Abbreviations

SiC	Silicon carbide
SFs	Stacking faults
BJT	Bipolar junction transistor
HCP	Hexagonal close-packed
BPD	Basal plane dislocation
SEM	Scanning electron microscopy
TEM	Transmission electron microscopy
LED	Light emitting diode
TSD	Threading screw dislocation
TED	Threading edge dislocation
MOSFET	Metal oxide semiconductor field effect transistor

Symbols

n	Electron concentration
p	Hole concentration
n	Ideality factor
D	Diffusivity
μ	Mobility
k_B	Boltzmann constant

Chapter 1

Introduction to Silicon Carbide

1.1 A General Introduction to Silicon Carbide

Silicon carbide is a compound semiconductor. Given its nature of strong mostly covalent bonding between silicon and carbon atom, it has good stability under high radiation and chemical environments [1-2].

Silicon carbide is also one of the third-generation semiconductors, along with gallium nitride, zinc oxide and some other wide bandgap semiconductors, are promising materials that can be used for current and future power conversion and energy network [3].

This feature of wide band gap in SiC polytypes makes it suitable for high temperature application and allows a control of a wide service temperature due to low intrinsic carrier concentration [4]. Compared to silicon, the band gap and electric break down field is many times higher in silicon carbide [5]. Applications of silicon carbide in devices such as metal oxide semiconductor field effect transistors (MOSFET) and bipolar junction transistors (BJT) have proven its value in power electrons [6-9].

In addition to the benefit of high switching frequency and break down voltage [4], the wide band gap of silicon carbide also allows it to emit photon at a variety of visible wavelengths that corresponds to the band gap energy of the silicon carbide polytypes [10-12]. Despite the early discovery of the electroluminescence of silicon carbide in 1907, other group III-V compound semiconductors soon replaced SiC for the purpose of electroluminescence due to the combined factor from the matured fabrication process of epitaxial growth and the nature of direct band gap [13].

Another limitation of SiC applications in the LED industry and power electronics is the device instability caused by crystallographic defects such as deep level colour centers, partial or perfect dislocations, stacking faults and many others [14-17]. The generation mechanism of defects and their effects on the device stability will be discussed in the next chapter.

1.2 Silicon Carbide Polytypes

As a compound semiconductor, silicon carbide has more than 250 polytypes in nature, such property is called polytypism [18]. The stacking sequence of silicon carbide bilayers and the form of the crystal structure varies between each polytype. Among all the polytypes, 3C-SiC, 6H-SiC and 4H-SiC are the most commercially available [2, 8]. Based on Ramsdell notation, 3C-SiC has a simple cubic (SC) crystal structure as shown in Figure 1.1 on the left with a repeating sequence of ABC, whereas 4H-SiC and 6H-SiC has hexagonal close-packed (HCP) crystal structure as shown in Figure 1.1 on the right where the stacking sequence each varies from ABCB to ABCACB.

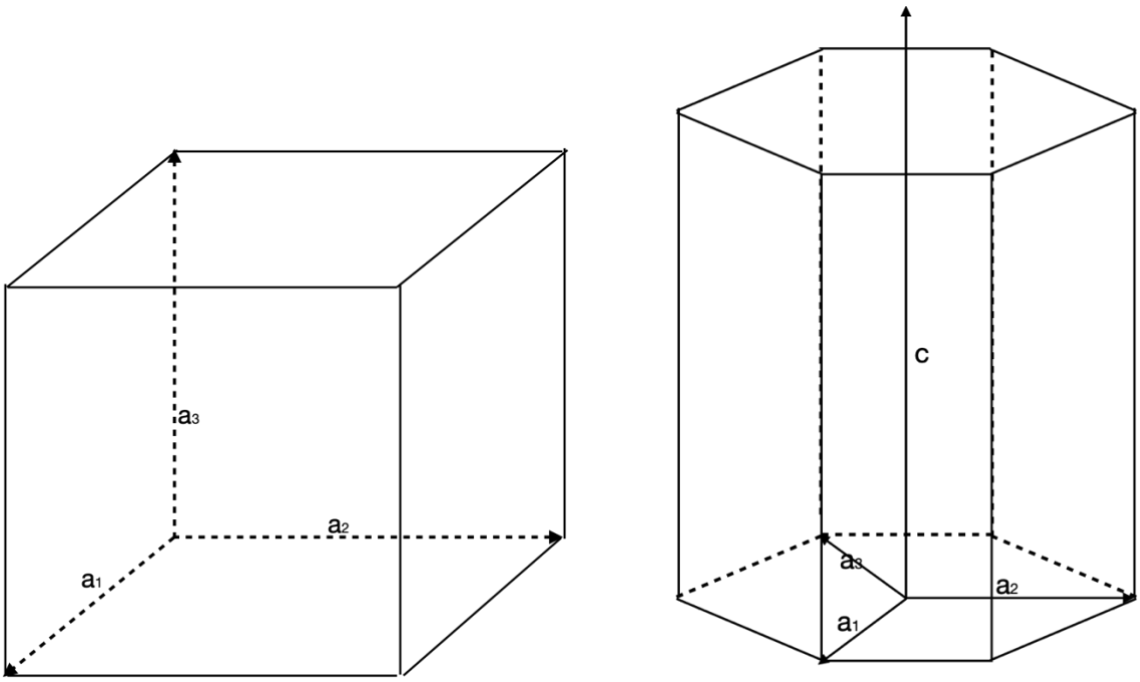

Figure 1.1: A typical cubic structure and hexagonal structure

Different from the cubic structure, a hexagonal structure representation is usually in the four index system, where four axes: a_1, a_2, a_3 and c are used to identify the plane system and direction.

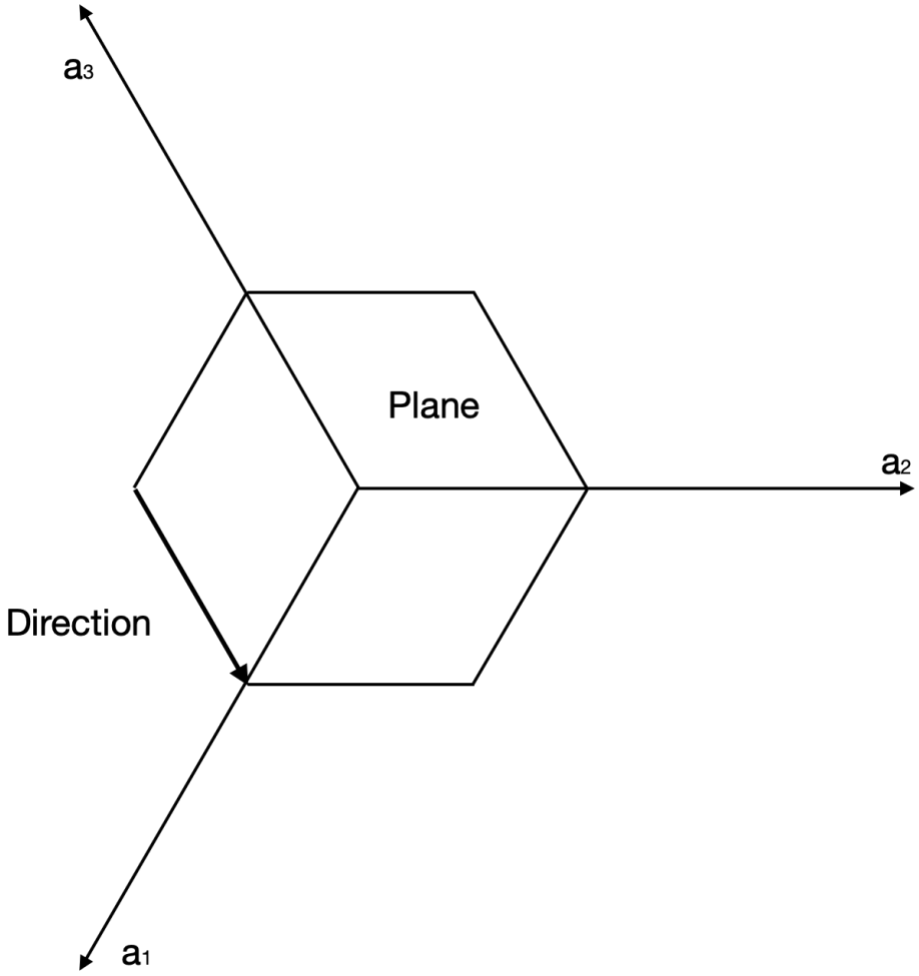

Figure 1.2: Four index system of a hexagonal structure

The miller indices of a direction inside the four index system can be converted from the [UVW] in three index system into [uvtw]. Similarly, for a plane (hkl), its miller indices in four axis system can be converted into (hkil). For instance, for a direction in the three index system with miller indices [110], as the darkened line in Figure 1.2:

$$u = \frac{n}{3}(2U - V) = \frac{n}{3}(2 - 1) = \frac{n}{3} \tag{1.1}$$

$$v = \frac{n}{3}(2V - U) = \frac{n}{3}(2 - 1) = \frac{n}{3} \tag{1.2}$$

$$t = -(U + V) = -(1 + 1) = -2 \tag{1.3}$$

$$w = nW = 0 \tag{1.4}$$

where n is used to reduce u,v and t into the smallest integer number. By following the calculation, the direction [110] in the four index system will be [11-20].

For a plane with miller indices (1-10):

$$h = h = 1 \tag{1.5}$$

$$k = k = -1 \tag{1.6}$$

$$i = -(h + k) = -(1 - 1) = 0 \tag{1.7}$$

$$l = l = 0 \tag{1.8}$$

Therefore, the plane (1-10) is now transformed into (1-100) in the four index system. If the direction [UVW] lies on plane (hkl), the miller indices of the direction and plane also follow the relationship of: $Uh + Vk + Wl = uh + vk + ti + wl = 0$.

The planes a, m and basal plane are colour coded in light grey, dark grey and grey in Figure 1.3 with miller indices of (2-1-10), (0-110) and (0001). Both a and m planes belong to the prism slip system, whereas the basal plane is the closed-pack plane in the hexagonal system.

Because the silicon carbide epitaxial layer is typically fabricated on or off axis of the (0001) substrate plane [19], defects on basal plane can severely influence the device stability if it locates close to the junction. A more detailed discussion about basal plane dislocation will be introduced in Chapter 2.

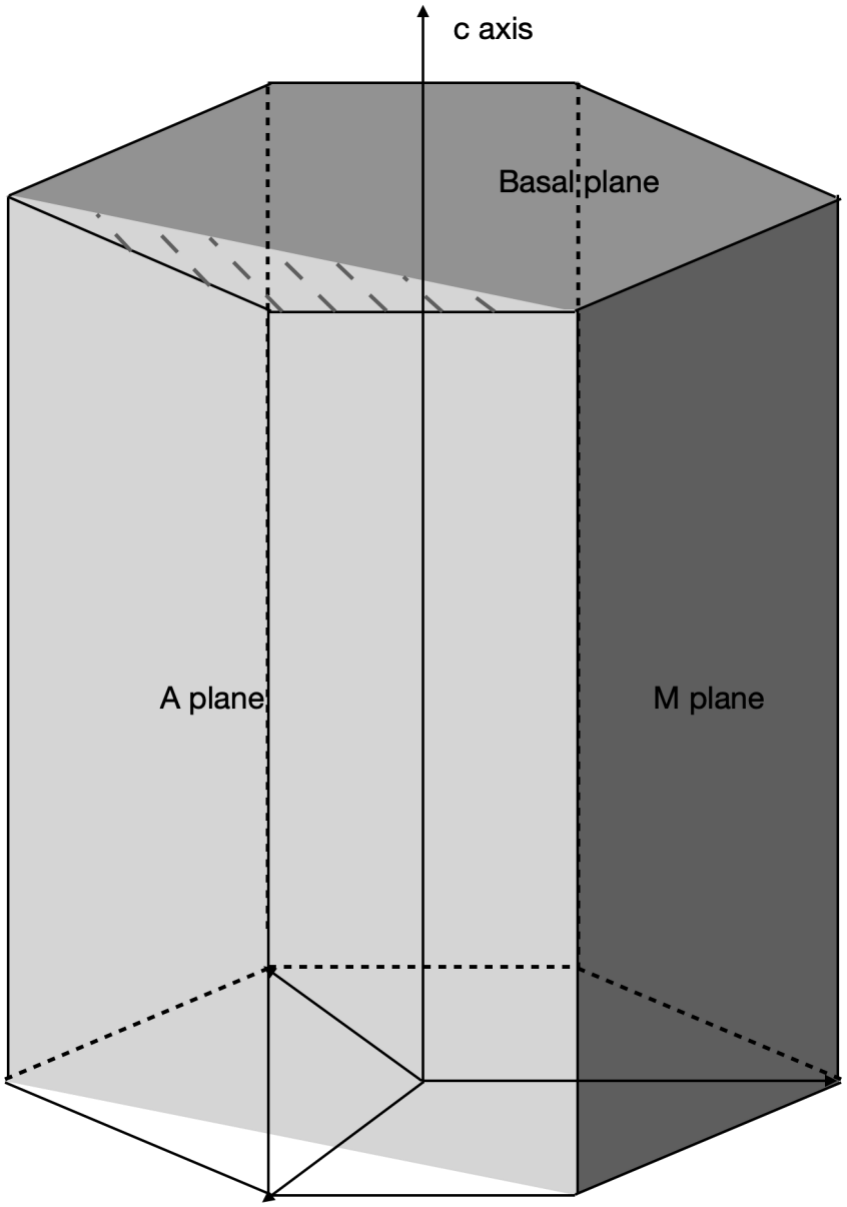

Figure 1.3: Planes of hexagonal silicon carbide polytypes

1.3 Material Properties of Silicon Carbide

SiC has a tetrahedral bonding between carbon and silicon atoms, even with the same chemical composition of half carbon and half silicon, each polytype has its own unique material properties.

Table 1.1 shows the material property of the most common three polytypes: 3C, 4H, and 6H [2, 18].

Property	3C-SiC	4H-SiC	6H-SiC
Bandgap E_g (eV), 300K	2.36	3.26	3.02
Lattice constant (Å)	4.36	a=3.09 c=10.08	a=3.09 c=15.12
Thermal conductivity ($W\ cm^{-1}K^{-1}$)	3-5	3-5	3-5
Relative permittivity	9.7	10	10
Hole mobility ($cm^2V^{-1}s^{-1}$)	40	120	90
Electron mobility ($cm^2V^{-1}s^{-1}$)	1000	//*c*-axis: 1200 ⊥*c*-axis: 1000	//*c*-axis: 100 ⊥*c*-axis: 450
Electron saturation velocity 10^7 ($cm\ s^{-1}$)	2.5	2	2

Table 1.1: Material properties of SiC polytypes

For 3C-SiC, only one lattice constant exists due to its simple cubic structure. For 4H- and 6H- SiC, however, as a result from the larger distance between each atom along the c axis, the material property is anisotropic [18]. In this paper, 4H-SiC is studied because it is commonly applied to the power electronic industry [20-21] due to its outstanding properties in carrier mobility and relatively low anisotropy compared to 6H-SiC [17] and good stability at high temperature compared to 3C-SiC as 3C-SiC may transform into 6H-SiC when temperature is above 2150 ºC [22].

The wide band gap gives two major benefits to SiC application, one is that SiC polytypes have lower intrinsic carrier concentration at room temperature, which is on the order of 10^{-9} cm^{-3} compared to other common semiconductors [16].

Another benefit is that it gives SiC polytypes a trait of photon emission at a range of visible wavelengths. For 3C-, 4H- and 6H-SiC, the band gaps of 2.36, 3.26 and 3.02 eV have a corresponding wavelengths of photon emission at approximately 525, 380 and 410 nm, respectively. Owing to the small energy difference between each polytype, a variation of stacking sequence is frequently observed from silicon carbide bulk material [23]. This distinction of emitted photon wavelength can help identify polytype inclusions inside the matrix.

Figure 1.4 shows a semiconductor with a direct band gap. When electrons from the conduction band recombine with the holes in the valence band, the photon emitted during the process has the same or very close to the amount of energy of the band gap of the material. In the case of 4H-SiC, with the band gap energy of 3.26 eV, if 4H-SiC were direct

band gap material, the wavelength of photon emitted due to band to band recombination should be close or equal to 380nm as previously discussed.

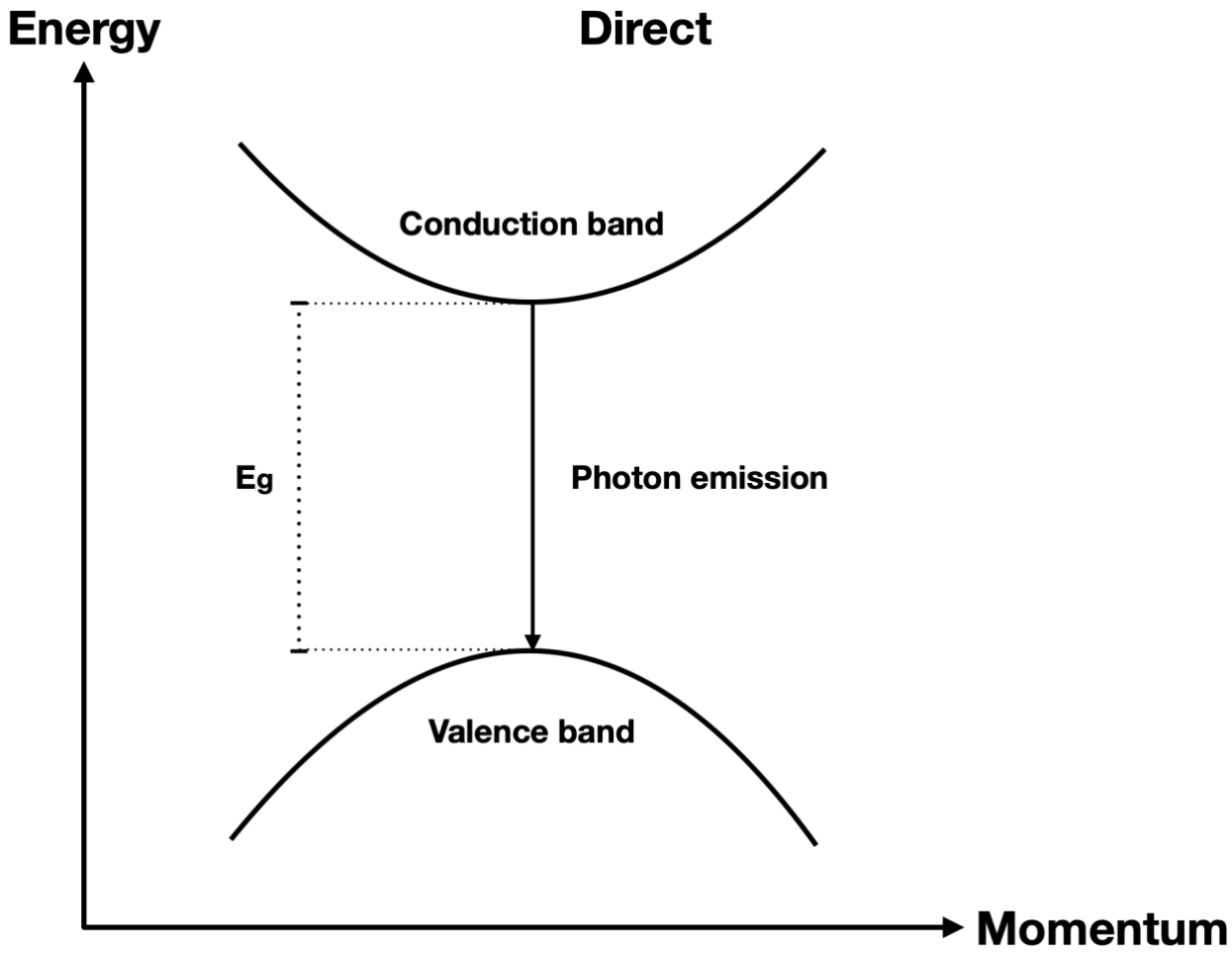

Figure 1.4: A simplified demonstration of direct band structure

The most common scenario of 4H-SiC spectra analysis, however, gives a strong peak at 390 nm, this is due to its nature of indirect band gap inside 4H-SiC. As shown in Figure 1.5, due to the misalignment between the top of valence band and the bottom of conduction band in k space, it requires phonon assistance for radiative recombination to occur. A relatively small amount of phonon energy will be used for crystal vibration to allow carriers to overcome the momentum difference and to radiatively recombine to emit photons.

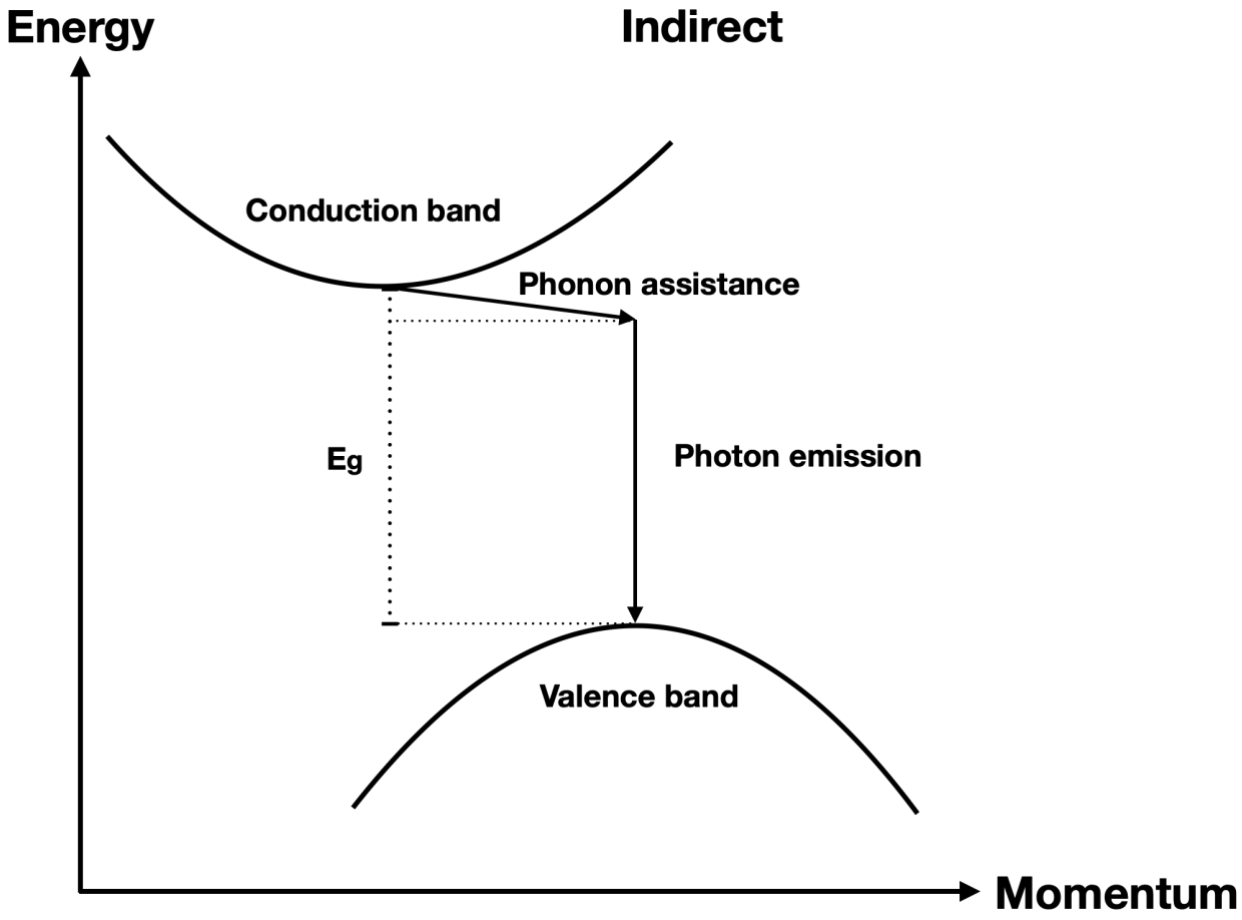

Figure 1.5: A simplified demonstration of indirect band structure

Due to the involvement of phonon energy, emitted photons will have lower energy compared to the band gap of the material and it will appear at a higher wavelength in the spectrum. As mentioned before, the 10 nm offset of spectrum peak in 4H-SiC from 380 nm to 390 nm is the result of phonon assistance[24]. In this work, this peak at 390 nm has been well observed for most of the samples and it will be discussed in later Chapters.

1.4 Silicon Carbide PN Junction and Bipolar Junction Transistor

A PN junction is a basic structure in a semiconductor component to supply carriers such as electrons and holes. The P region consists of a p type dopant (acceptor) that can be ionized to leave an unoccupied space (holes) where the N region release electrons from a n type dopant (donor). Due to the gradient of electron and hole concentration, carriers start to diffuse into the opposite region. Meanwhile, since the dopant from both sides are ionized near the junction interface, a built in potential is induced and creates a space charged region that motivates carriers to start to drift. At the condition where no external forces are present (such as radiation and electrical field), the carrier drift will counter the diffusion to reach an equilibrium with a formation of a depletion layer.

For any typical LED, a forward bias is applied to the junction for carriers to constantly radiatively recombine.

In this paper, to study the effects of defects on the material, several 4H-SiC BJT sample from GeneSiC are tested with EL spectra and IV characteristics under forward bias. The minority carrier lifetime in 4H-SiC is controllable by using several types of treatments [25-26] as Table 1.2 indicates. Electron and hole diffusivity are calculated based on Einstein relation [27]:

$$D = \frac{\kappa_B T}{q}\mu \tag{1.9}$$

where D is the diffusivity of carriers calculated based on k_B (Boltzmann's constant) T (Temperature), q (electric charge) and μ (carrier mobility). The value of μ is taken from Table 1.1. Diffusion length is calculated by:

$$L = \sqrt{D\tau} \tag{1.10}$$

Where L is the diffusion length of carriers, τ is the carrier lifetime.

Sample type	Directions	4H		4H	
Treatment		Thermal [25]		Carbon-implantation/ Annealing [26]	
		without	with	without	with
Carrier lifetime (μs)		0.69	9.5	3.5	18.5
Electron Diffusivity Dn* (cm^2s^{-1})	//c-axis:	31.2	31.2	31.2	31.2
	⊥c-axis:	26	26	26	26
Diffusion length Ln (μm)	//c-axis:	46.4	172	104	240
	⊥c-axis:	42.4	157	95.4	219
Hole Diffusivity Dp* (cm^2s^{-1})		3.12	3.12	3.12	3.12
Diffusion length Lp (μm)		14.7	54.4	33	76

*At T= 300K

Table 1.2: Lifetime and diffusion length of minority carriers in 4H-SiC under different treatment

One feature of the as received SiC BJT sample, is the interdigitated structure as shown in Figure 1.6:

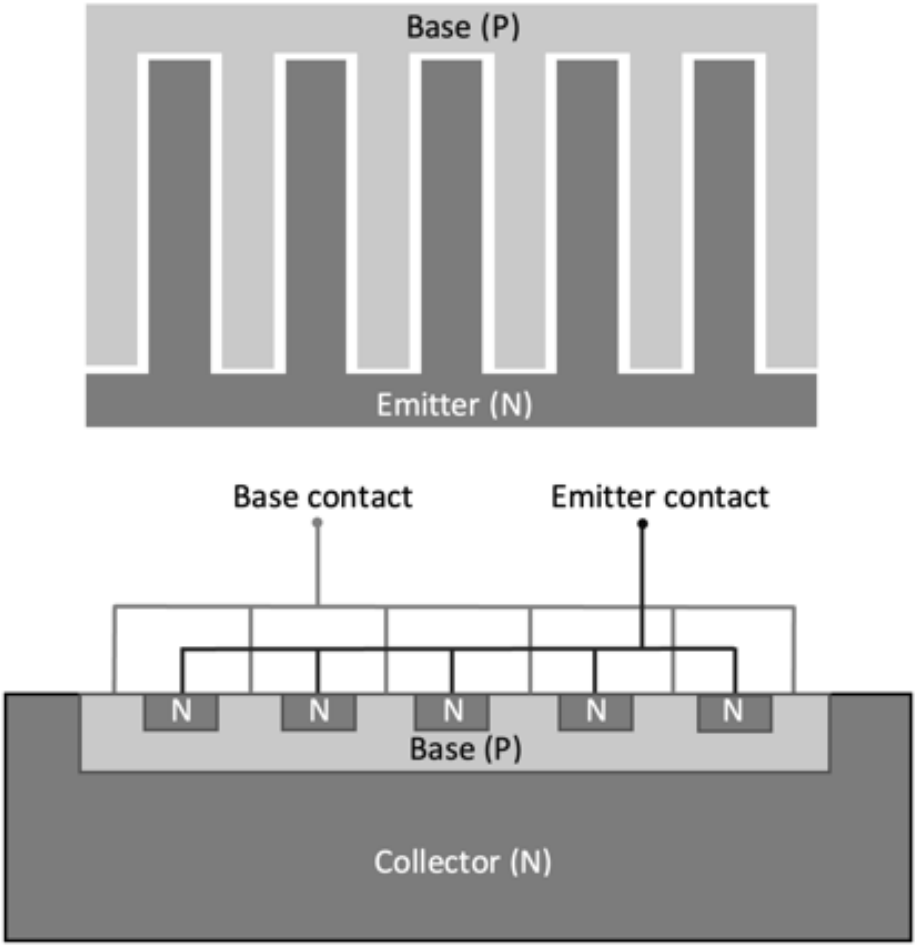

Figure 1.6: A demonstration of interdigitation in BJT

A typical BJT consists of three junctions: base, emitter, and collector. In this interdigitated structure, the base (p-type) and emitter (n-type) intersect with each other periodically.

The electrodes connection is on the top of both base and emitter junctions. A n-type collector is located underneath such interdigitations. Such structure allows more efficient and uniform carrier flow as the area of the interface between the PN junction are greatly increased.

In Chapter 4, such a structure can be observed in the optical image due to the radiative recombination at the active junction area during the device operation.

Chapter 2

Defect Mechanism and Characterization in Silicon Carbide

2.1 Major Extended Defects in Silicon Carbide

SiC has been well developed since the advent of epitaxial growth technique for compound semiconductor production [28-30]. The existence of defects is still quite inevitable as the presence of defects at the substrate is commonly observed [31], but a high quality wafer with low dislocation density can be obtained by using a homoepitaxial growth technique [32].

The extension and conversion of defects from the substrate to the epilayers can occur during fabrication [33, 34], thus, the reduction of the defect density on substrate is crucial for many silicon carbide applications.

Major extended defects that negatively affect device performance are shown in Table 2.1 [16, 18]:

Type of defects	Direction
Micropipe	[0001]
Threading screw dislocation (TSD)	[0001]
Threading edge dislocation (TED)	[0001]
Stacking faults (SFs)	On (0001) plane
Basal plane dislocation (BPD)	Likely [11-20]

Table 2.1: Major extended defects inside silicon carbide

The density of micropipes has been greatly reduced with current epitaxial growth technology since it causes severe device degradation more than other extended defects with the size in the level of micrometer [35].

As mentioned in Chapter 1, the Miller indices of defects growth direction and location are vital for one to analyse their effects to the material property and device performance. As in the case of micropipes, threading screw dislocation (TSD) and threading edge dislocation (TED), are all grow along the c-axis [0001]. They can penetrate the bulk material from to the substrate easily due to the alignment with the growth direction [36, 37].

As the name indicates, a basal plane dislocation (BPD), lies on the basal plane (0001). It can be located between active junctions and can degrade the diode and increases the leakage current [38-39]. BPD has a similar structure compared to TED, and due to the similarity, the conversion between those two dislocations is commonly observed [34]. The different growth direction, however, makes it harder for a basal plane dislocation located in the substrate to propagate into the epitaxial material [36].

Plastic deformation causes nucleation of BPD with a preferred slip direction along [11-20]. This could result in an extra or missing half plane which originates stacking faults [16].

2.2 Stacking Faults

Stacking faults may originate from defects like TSD and BPD during epitaxial crystal growth or be induced by carrier recombination during device operation [40-42]. The low formation energy of stacking faults in silicon carbide makes it more likely to be observed in silicon carbide polytypes compared to other semiconductor [41], however, the cause of this is yet unknown. In general, stacking faults can be regards as inclusions of other polytypes or a planer defect that have a distinctive stacking sequence compared to the bulk material.

The structure of the band gap varies depending on the crystal orientation where the band gap energy at the stacking faults is lower compared to the matrix [43-45]. Stacking faults can therefore behave like a radiative recombination center as the carriers preferably recombine at lower energy [46]. This not only increases the resistance of the device and the

leakage current but also reduces carrier lifetime and strongly confines the carriers at one dimension [18].

The generation mechanism of stacking faults is well studied by many : Stacking fault can be generated during CVD when a perfect basal plane dislocation dissociates into two partial dislocations and in-between which, stacking faults is formed [47]. Frank type stacking faults can be generated due to a low ratio conversion from TSD during fabrication [48]. An intrinsic and extrinsic dislocation loop that encloses stacking faults are as shown in Figure 2.1.

Besides being generated during epitaxial growth, recombination induced dislocation glide could also cause stacking faults extension [40,43].

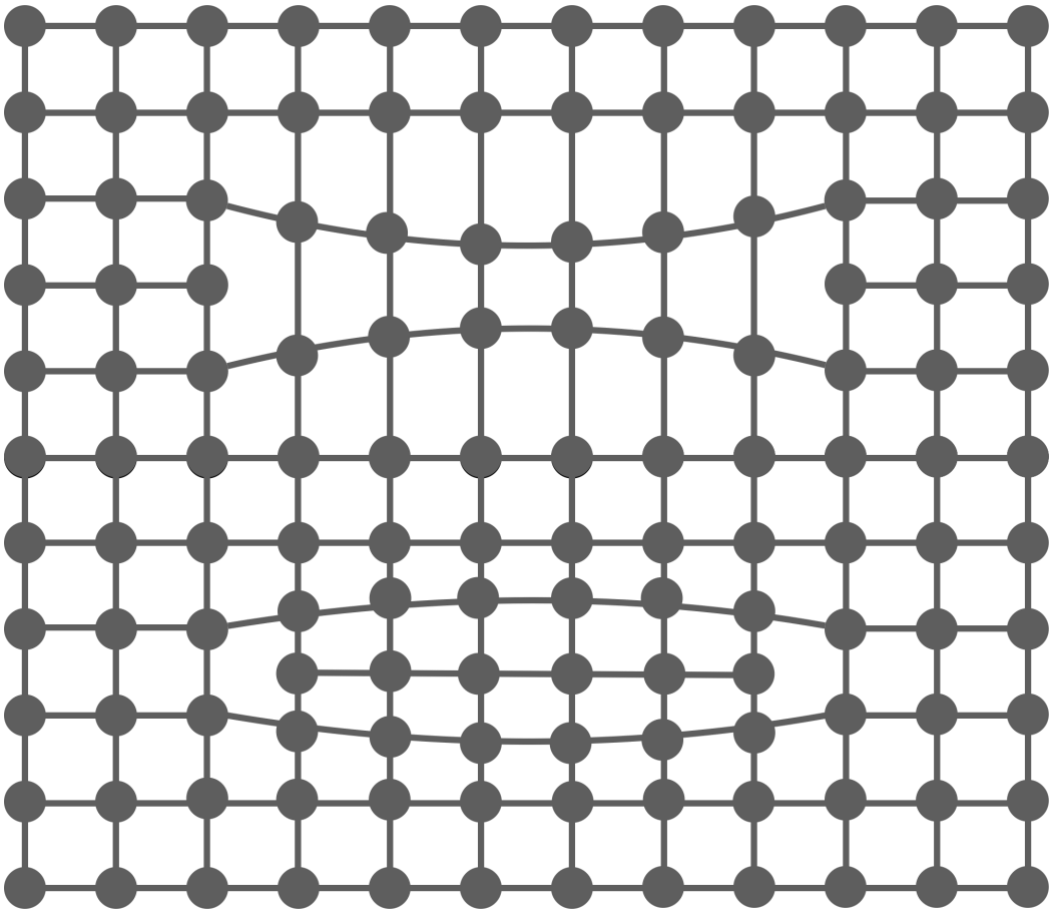

Figure 2.1: A simplified diagram showing an intrinsic dislocation loop (top) and an extrinsic dislocation loop (bottom) that encloses stacking faults

2.3 Surface Defects

In addition to the bulk defects inside SiC, surface defects are also commonly observed. Defects such as carrot defect, triangular defects and pits all belong to this category [49-50]. Some of the surface defects are composed by other defects, for instance, a triangular defect may be constructed by a 3C inclusion inside other polytypes [51-52].

Surface defects also reduce carrier lifetime, where carriers can be attracted and recombine over the region [53]. In the case of a thin film, if the carrier diffusion length is relatively long, surface recombination could be the main cause of carrier lifetime reduction [54].

Surface passivation can be a useful tool to reduce surface recombination by changing the carrier concentration at the surface [25,55]. The effect of passivation on the carrier lifetime can be seen in Chapter 1 Table 1.2. The use of guard rings to prevent surface recombination is also observed in as received sample.

Optical excitation can also be observed from some of the surface recombination, such that surface defects generated by electrochemical etching may cause radiative recombination [56-57]. A white light can be obtained after passivation with aluminum oxide from a porous silicon carbide [58], where an emission of a blue colour (460 nm) from the oxygen vacancies and a green (530 nm) emission from carbon related surface defects were obtained by using anodic etching with HF solution to the silicon carbide.

In this paper, the effect of surface defects that are generated by chemical etching on the sample EL spectra are discussed in Chapter 3.

2.4 Defects Characterization

The basic idea of defect characterization is either to detect the photon emission over the faulted region or analyse the interference pattern of the diffracted beam (electron or X-ray). Extended defects and some of the surface defects can be detected by electro and photoluminescence owing to their optical properties. The band structure varies from the matrix due to the presence of those defects where the local band gap energy is lower compared to the bulk, or else a mid-band gap energy level is generated. Therefore, the radiative recombination inside the faulted area usually emits photons at a lower energy and at a higher wavelength such that an extra or dominate emission peak will appear distinct from the band to band emission in the EL/PL spectra [33, 59, 60].

For instance, in the presence of TSD, a 750-900 nm infrared emission peak is expected [61]. Where in the case of stacking faults, depending on the variation of the stacking sequence, it has different emission peak as Table 1.2 indicates [41]:

Type of stacking faults	1SSF Intrinsic Frank SFs	2SSF	3SSF	4SSF
Emission peak (nm)	420	500	480	455-460
Photon energy (eV)	2.95	2.48	2.58	2.70

Table 2.2: Emission peak of varies stacking faults

Transmission electron microscopy (TEM) is another method commonly used to detect extended defects inside material, as the perfect crystal orientation is destroyed at the vicinity of the defects, high resolution transmission electron microscopy (HRTEM) can help identify and locate the defects by directly showing the crystalline structure from the image which is created based on the interference pattern of the diffracted electron beam [62].

An indirect method to detect stacking fault formation is by testing sample IV characteristic. From the derivation of diode equation, ideality factor *n* follows the relationship :

$$I \propto I_0 \cdot \exp\left(\frac{qv}{nkT}\right) \tag{2.1}$$

where *n* can be determined by the slope of the log *I* vs V curve. From the study of compound III-V LED material, a value of *n* that is greater than 2 is often observed from the diode that has a quantum well structure [63].

Since stacking faults also have a quantum confinement effect on the carriers, therefore, a similar IV characteristic is expected for the sample with SFs present.

Other common methods including cathodoluminescence, atomic force microscopy, x-ray topography and etching pit are also useful for characterizing and locate extended defects inside material [64-67].

In this work, electroluminescence spectra testing and IV characterization are used to detect defects.

Chapter 3

Effect of Surface Etching on Spectrum of 4H-SiC

3.1 Sample Preparation and Spectrum Testing

Four SiC samples before and after anodic etching were tested. The purpose of this test is to detect the effect of etching on a SiC recombination mechanism. The EL spectrum and IV characteristics are tested by means of the following steps:

1. Surface exposure:

Four 4H-SiC BJT samples GA05JT12-263, purchased from GenenSiC are tested.

The bare die is embedded inside the package and on top of a copper contact. Since a clear light output must be seen from the exposed surface to test sample EL spectra, all samples were cut open with a diamond blade to allow light to exit from the exposed side wall. The sample was connected to a DC power supply (MTP DC POWER SUPPLY 5003) at 0.2 A while taking the image as Figure 3.1 illustrates:

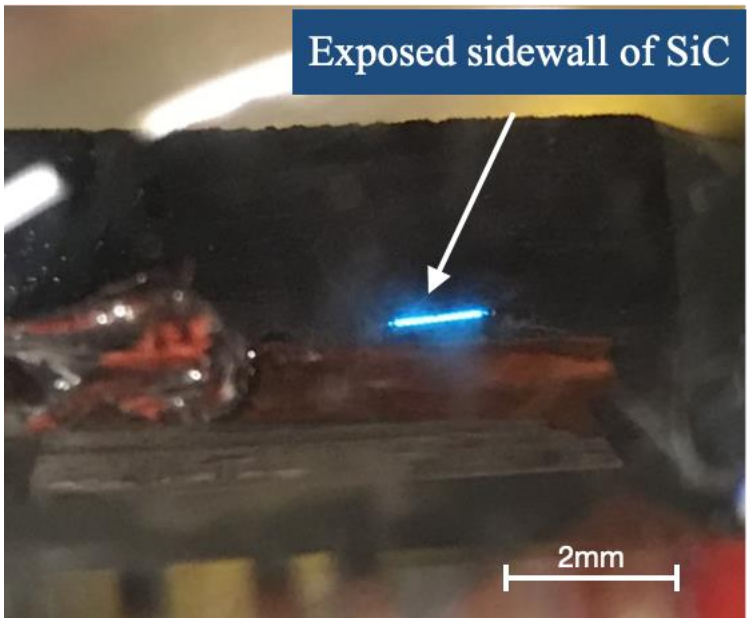

Figure 3.1: Exposed bare die of 4H-SiC BJT sample.

2.Spectrum testing

After surface exposure, the bare die is ready to be tested by the acquisition of the EL spectra. The overall set up for spectra testing is illustrated as below:

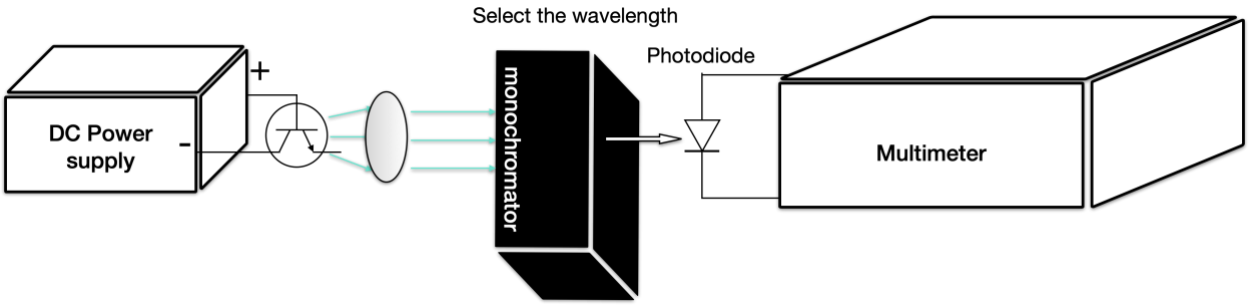

Figure 3.2: Set up of spectrum testing

All BJT samples were connected with a DC power supply at 0.2 A during EL spectra testing. Light exited from the exposed surface was focused by a lens to enter the monochromator (Optometrics Digital Mini-Chrom monochromator DMC1-03). Where wavelength was selected. Once the light beam exited the monochromator, it was collected by a photodiode (THORLABS inc 201/579-7227) and the relative intensity was shown on the multimeter (HEWLETT PACKARD 34401A) with respect to each wavelength. The range of wavelengths was selected to be from 370 nm to 600 nm as the majority of the peak in 4H-SiC spectra are around 390 nm (phonon assisted band to band).

3.IV testing

IV behavior of Samples 3 and 4 before and after etching were collected by the multimeter.

4.SiC surface etching

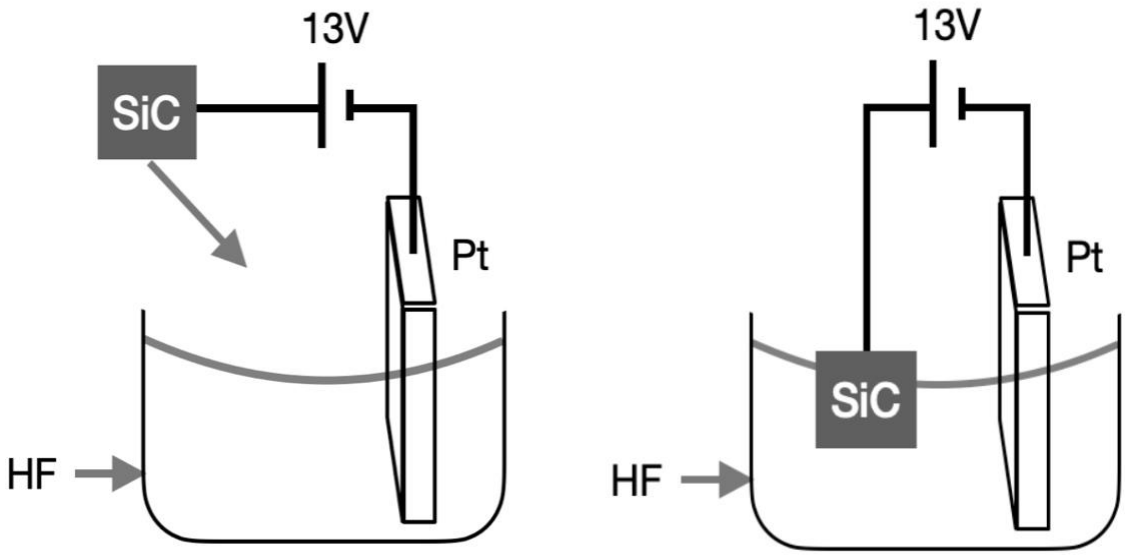

Figure 3.3: A demonstration of anodic etching process

As shown in Figure 3.3, each SiC sample underwent same anodic etching to produce a porous region by using a solution contain 20% concentrated hydrofluoric acid, 75% distilled water and 5% ethanol by volume. SiC samples were connected with a platinum plate to a DC power supply at 13 V for 4 minutes.

5.Image

SEM images shown in Figure 3.4 were taken for analyzing the length of the porous region.

3.2 Data and Observations

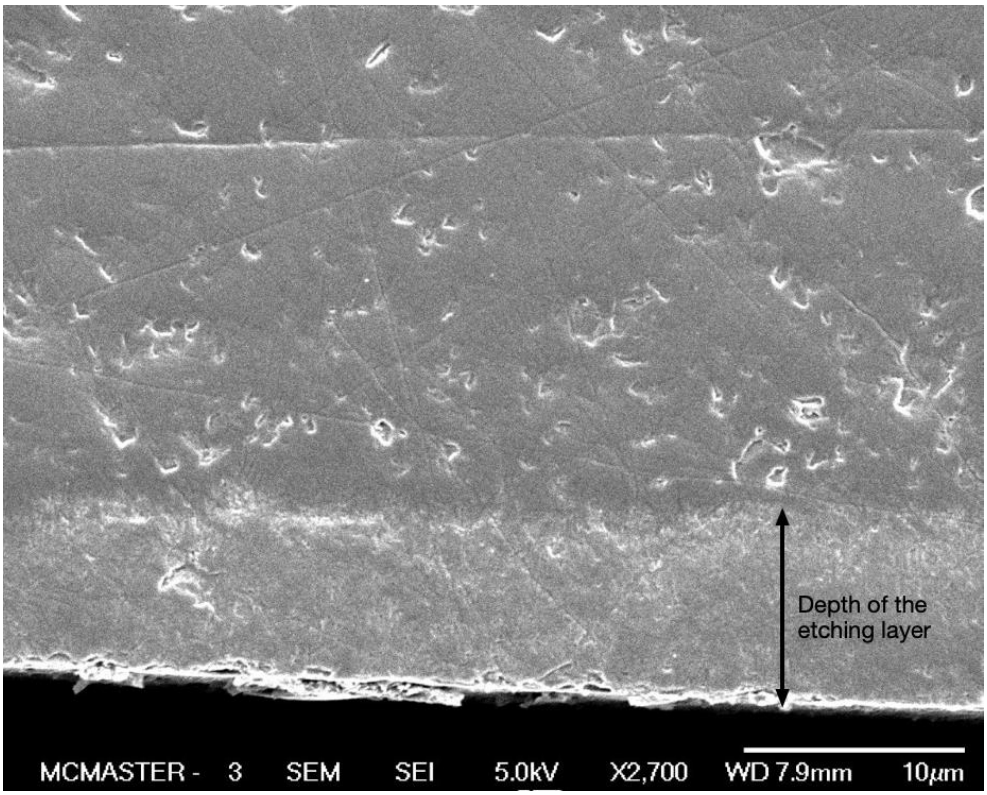

Figure 3.4: SEM image showing the bare die at cross-section.

After anodic etching, a porous region from the top surface of the SiC chip appeared as the light-colored layer in Figure 3.4. The etching depth is assumed universal to all samples as the etching parameter is same for all samples.

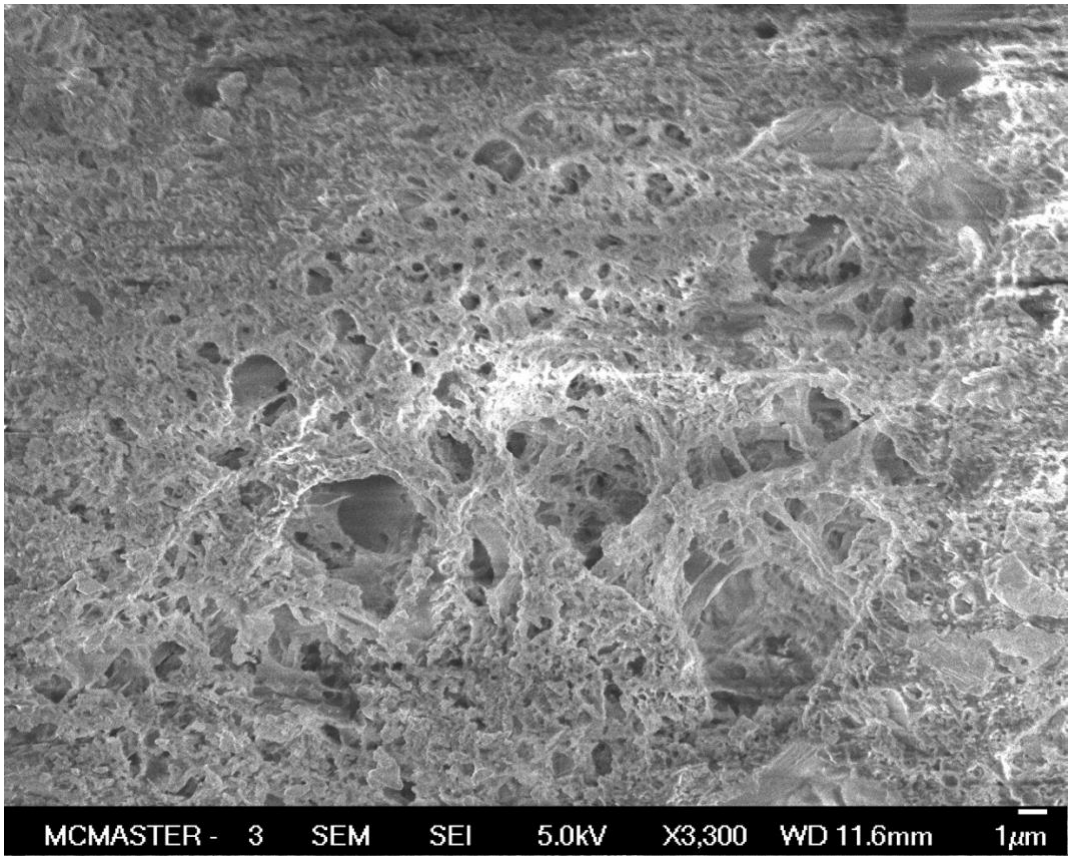

Figure 3.5: SEM image showing the porous region

Figure 3.5 shows the SEM image of the porous region from the front view. Surface defects such as dangling bonds and vacancies are highly expected.

Spectrum results:

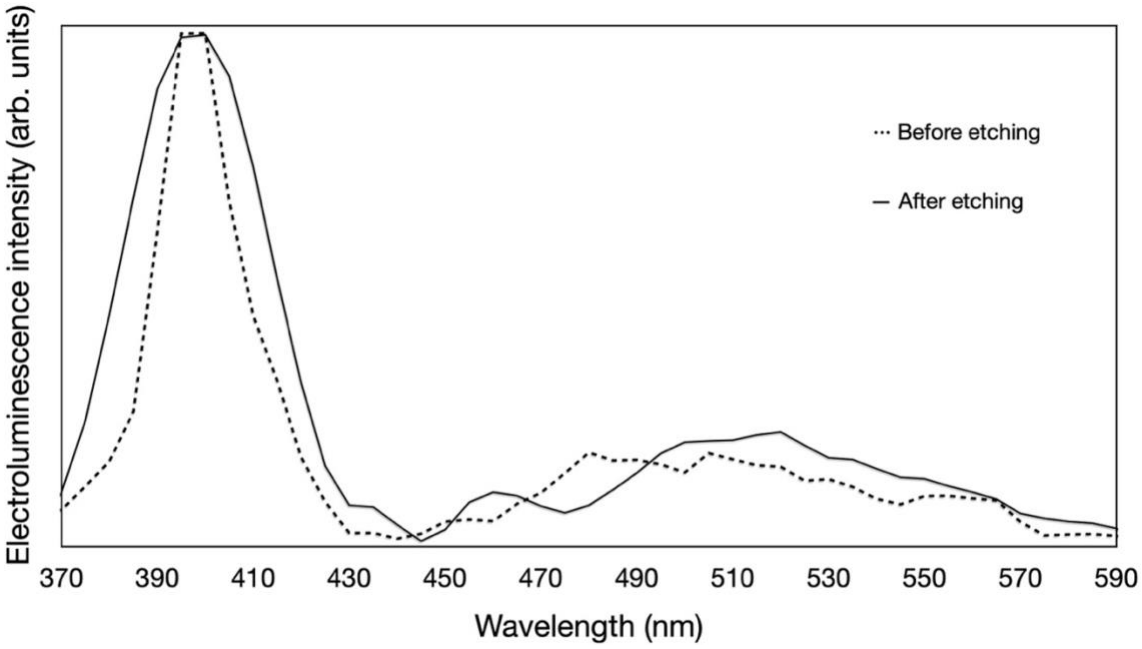

Figure 3.6: Spectrum of sample 1 before and after etching

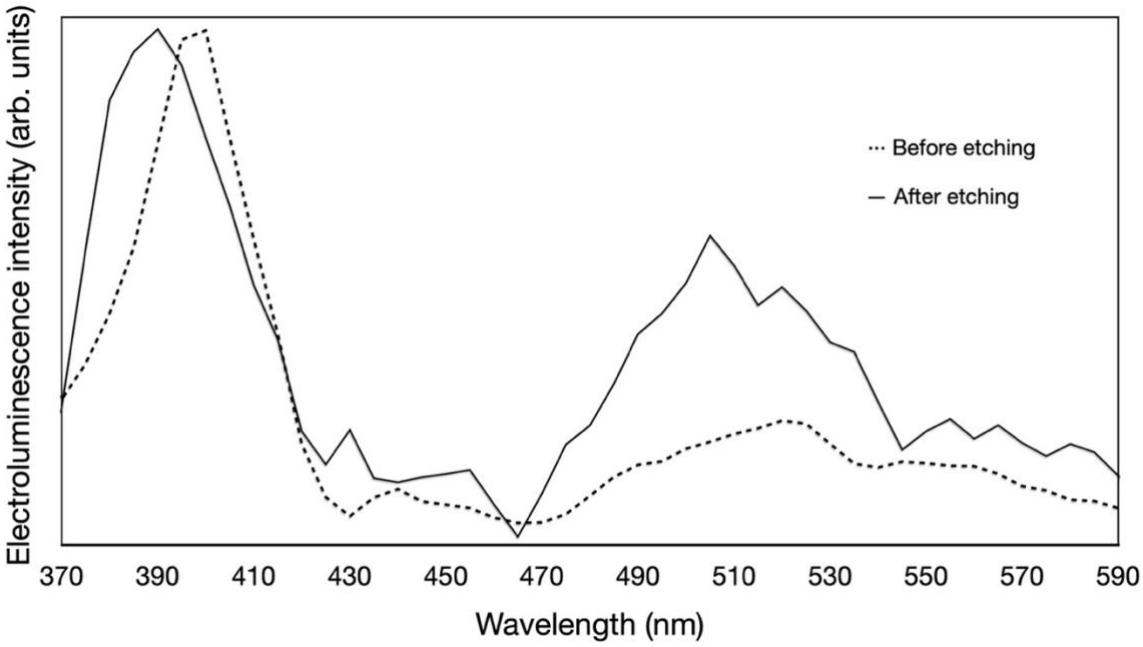

Figure 3.7: Spectrum of sample 2 before and after etching

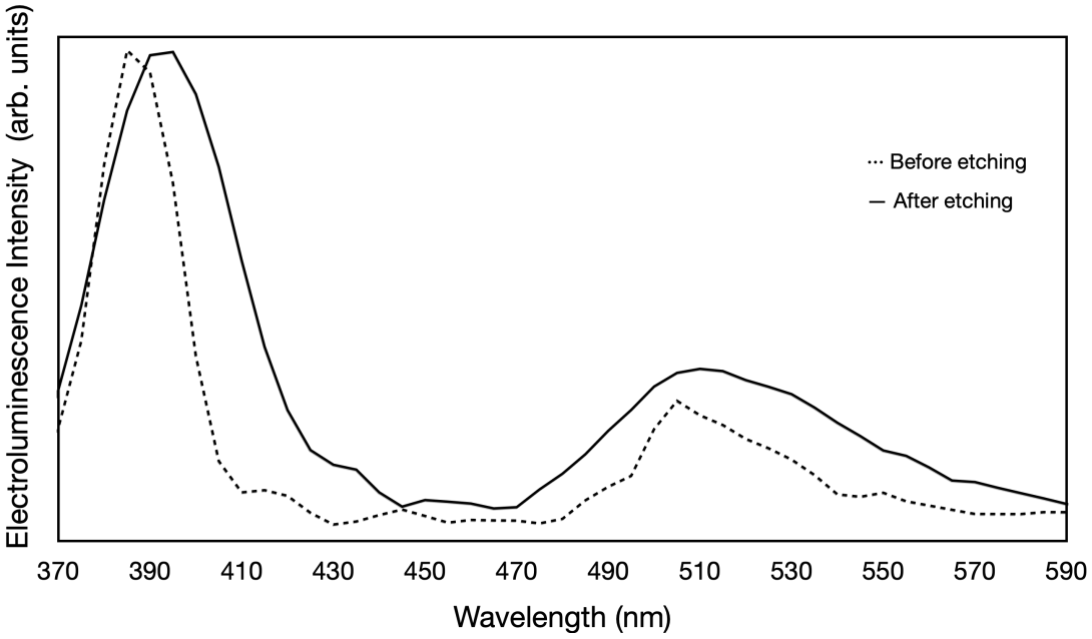

Figure 3.8: Spectrum of sample 3 before and after etching

The spectrum of Sample 4 is not presented in Chapter 3 due to the observation of stacking faults formation inside the sample. It will be presented in Chapter 5.

3.3 Analysis

1. Spectrum analysis

From the Figure 3.4, the depth of the etching layer from the exposed surface is approximately 8 to 9 micrometers. Figure 3.6 shows spectra of Sample 1 before and after etching with a strong peak near 390 nm which indicates phonon assisted band to band recombination.

In addition to that, Figure 3.6 also shows a peak centered at 500 nm as a broad green emission. The cause of this emission before etching is, as of now, not determined from the literature; one assumption is the boron related point defect, which gives photon emission at 510 nm [68] but does not really explain the intensity. Another is the carbon core partial dislocations that gives photon emission at 530 to 540 nm [14] which does not really match the 500 nm peak center.

One unique feature in our as-received sample, however, is the interdigitation of the junction, which may be the cause of this emission. Considering the stacking sequence may vary at some of the junction interface due to different dopant and doping level with small thickness. From the literature review in Chapter 2, recombination due to carbon related surface defects at the porous region would also cause green light emission [58]. As expected, all samples show an increased emission around this green region after anodic etching, but the change of intensity is not universal.

Further analysis suggests this is the result from the distinction on surface treatment as a guard ring was used by the manufacturer to prevent surface recombination.

In the case of Sample 2, a rougher and deeply ground surface gives the porous region a direct proximity to the active junction compared to Sample 1. This would allow a higher chance for carriers of both types (electrons or holes) to diffuse into the porous region and radiatively recombine over the recombination center introduced by the porous SiC.

Carrier diffusions are driven by the concentration gradient of the carriers injected across the p-n junction. The relative increase of green emission with respect to the overall intensity of peaks indicates only a small portion of carriers were able to diffuse into those regions. In addition to the spectrum testing, IV characteristics of Sample 3 were tested and presented in Table 3.1. Sample 3 was cut 50 micrometers away from the surface which is less than Sample 2 and this makes the porous region enter the active area. Similar to Sample 2, Sample 3 also shows an increase of green emission after the anodic etching.

Sample number	Treatment	Ideality factor**	Major recombination mechanisms in theory
Sample 1	Light surface exposure	-	Phonon assisted band to band recombination Dislocations/stacking faults
Sample 2	Deep surface exposure	-	Phonon assisted band to band recombination Dislocations/stacking faults, C-related defects
Sample 3	Intermediate surface exposure	1.320	Phonon assisted band to band recombination Dislocations/stacking faults, C-related defects
		1.390	

Table 3.1: Sample preparation and major recombination mechanisms

2. IV analysis

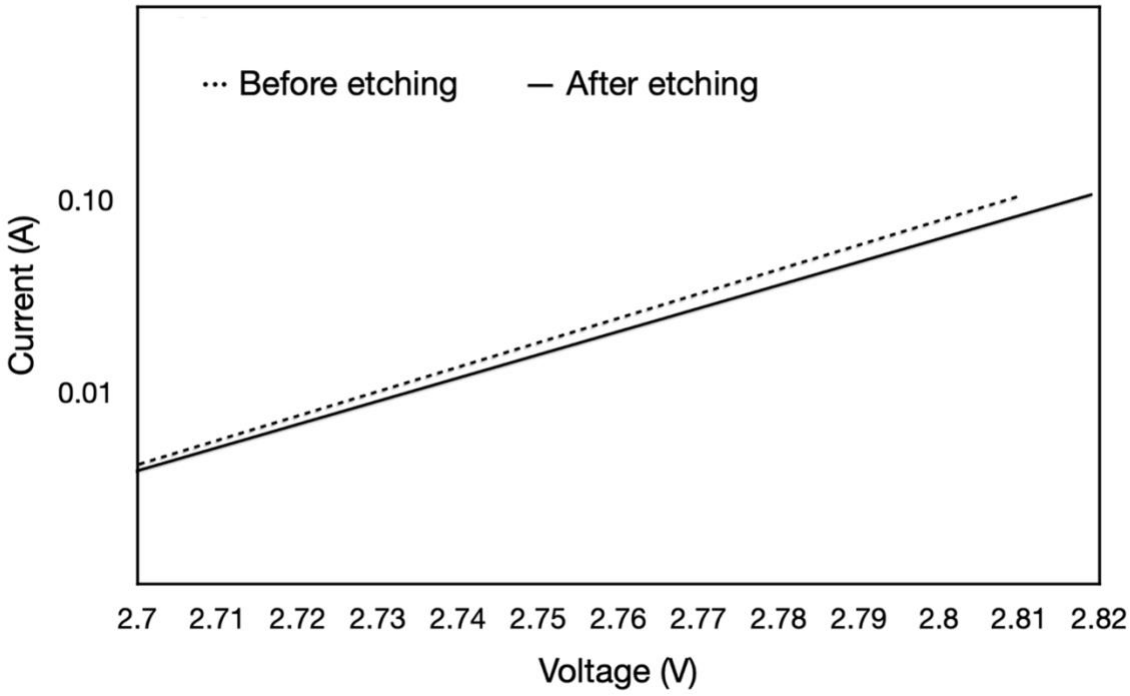

Figure 3.9: IV characteristics of sample 3 before and after etching in semi-log scale

For Sample 3, the IV characteristics are represented in semi-log scale for ideality factor analysis. As for the effect of anodic etching, Sample 3 has no significant difference on ideality factor. Part of the reason is because Sample 3 surface exposure is not too much so the carrier diffusion from the junction to the porous region are not too significant. Differently stated, for Sample 3, even after the etching, the majority of the carrier recombination still happens at the active junction area instead of the recombination center induced at the surface.

Chapter 4

Effect of Microindentation on Spectrum of 4H-SiC

4.1 Sample Preparation and Spectrum Testing

Three SiC samples before and after microindentation were tested for their EL spectra. The purpose of this experiment is to detect the effect of defects that were induced or influenced by the mechanical damage, on SiC EL spectrum and IV characteristics. The EL spectrum and IV were tested according to the following steps:

1. Surface exposure:

Three 4H-SiC BJT samples (GA20JT12-263), a newer version of 4H-SiC BJT sample (GA20JT12-263), purchased from GeneSiC are mounted into an epoxy pack for surface grinding and polishing. To obtain a clear surface, silicon carbide sandpapers with grit more than 600 were used. The sample is prepared either polished from the front (parallel to the interdigitation), or side polished (perpendicular to the interdigitation) as shown in appendix B. The structure of sample is similar as mentioned in Chapter 1. An oversimplified diagram of the polishing direction with respect to the junctions of each sample will be illustrated in the data and observation section.

2. Spectrum testing:

After the clear surface of the bare die was exposed, the EL spectra of each sample was tested before and after microindentation in two stages. The overall setting for spectrum testing is illustrated below:

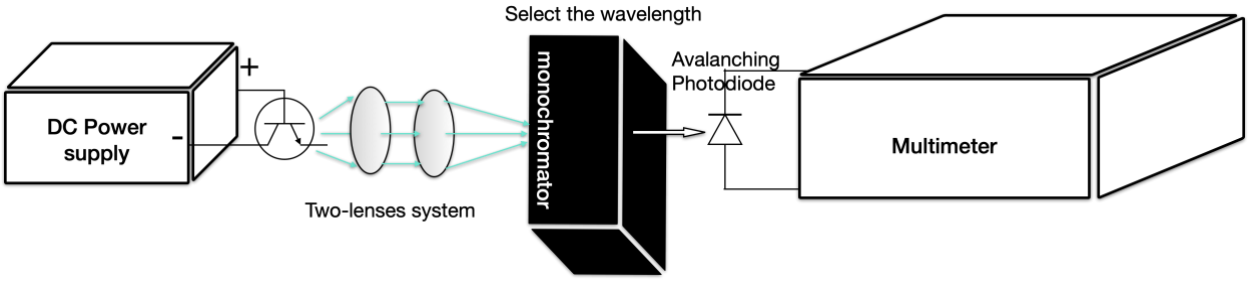

Figure 4.1: Improved setting of spectrum testing

Similar to the setting used in Chapter 3, all three samples were connected with a DC power supply (MTP DC POWER SUPPLY 5003) at 0.2 A. Light exited from the exposed surface was further focused by a two-lens system into the monochromator where wavelength were selected. Once the light beam exited the monochromator, it was collected by an avalanching photodiode which was connected to a multimeter (HEWLETT PACKARD 34401A) at 158 V. The relative intensity of all sample before and after each stage of indentation were collected from the multimeter with respect to each wavelength. The range of wavelength was selected to be from 370 nm to 600 nm, same as the previous test.

3. IV testing

IV behavior of Sample 2 and 3 before and after microindentations were collected by the multimeter.

4. Microindentation

After the EL spectra testing of the exposed sample, each sample was then subjected to a two stage microindentation. The load applied to the exposed sample surface and the number of microindentaions at each stage are listed in Table 4.1.

Sample Number	Exposed die edge	θ	Load (Gram-Force)	Number of Stage 1 Indentation	Total Number After Stage 2 Indentation
Sample 1	⊥ to interdigitations	90	300	7	13
Sample 2	Relatively ⊥ to interdigitations	100	200	11	22

Table 4.1: Sample preparation for microindentation

Sample 3 is not presented in Chapter 4 and will be discussed in Chapter 5 due to the observation of stacking faults.

4.2 Data and Observations

Optical images and spectrum results

In addition to the EL spectra of each sample, image illustrates the condition of the sample treatment is also included in this section along with optic microscopy image are also presented.

Sample 1:

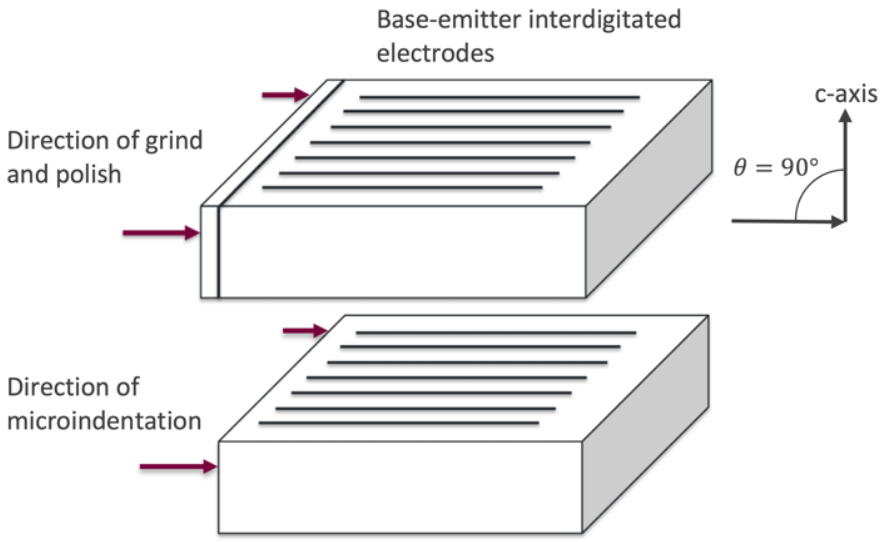

Figure 4.2: Structure of the sample 1 showing the direction of polish and grind with respect to the direction of microindentation.

Figure 4.2 shows the inside look of side polishing. The direction of grind and polish are perpendicular to the c-axis and parallel to the interdigitated electrodes. For Sample 1, the depth of grinding is not too deep as there was no observation of periodic light stripes corresponding to the interdigitated structure that was observed from the optical image of Sample 2 which will be shown in Figure 4.6.

After the second stage microindentation (total of 13 indents), the sample was connected to a power supply under an optical microscopy as Figure 4.3 illustrates:

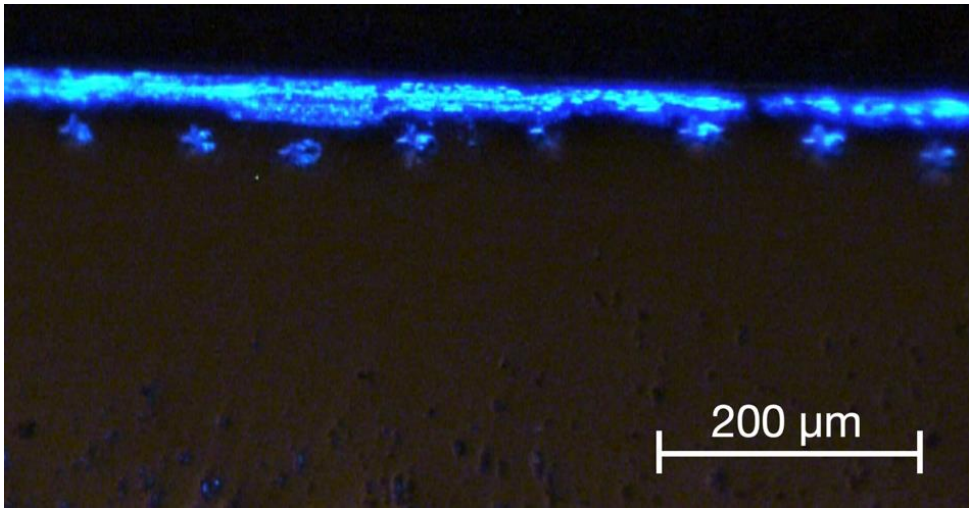

Figure 4.3: Optical image of sample 1 after microindentation with light visible from the microindentations.

Form the optical image of Sample 1, one can observe a clear light output from the microindentations. This light was taken into account as part of the EL spectrum after the indentation along with the light output from the non-faulted region exited from the top of the structure.

Notice the blue colour seen from the optical image is not the real colour, since the image was taken under a seperate light source from the optical microscope itself.

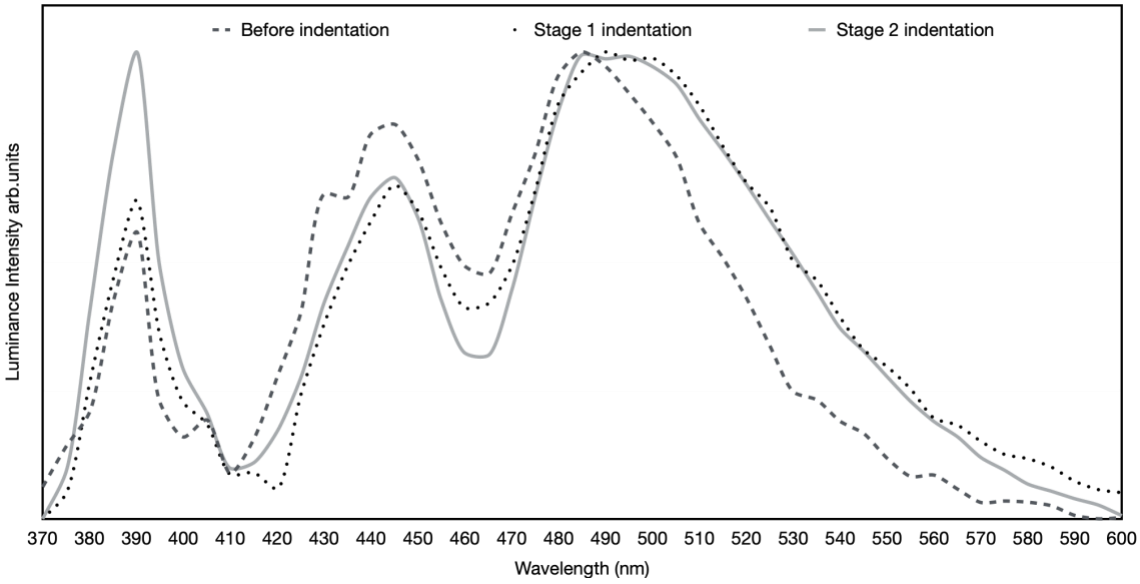

Figure 4.4: Spectrum of sample 1 before and after each indentation stages

EL spectra of Sample 1 under all stages of microindentations is superimposed into one image to analyse the change of the location, relative intensity and structure of emission peaks due to the external stress as shown in Figure 4.4. The 390 nm phonon assisted band to band recombination along with the 445 nm peak and a broad green emission are present in the spectrum of Sample 1 and 2.

Sample 2:

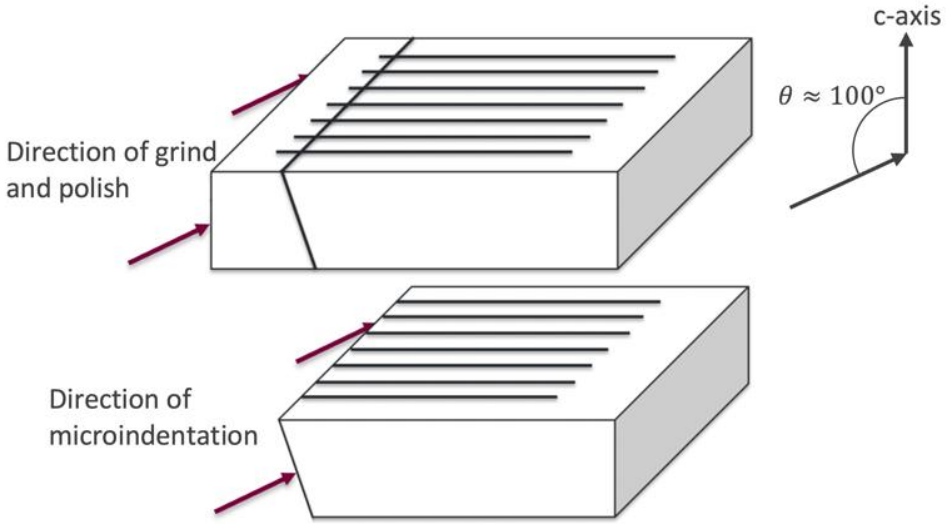

Figure 4.5: Structure of the sample 2 showing the direction of polish and grind with respect to the direction of microindentation

Figure 4.5 shows the inside look of another side polishing. The direction of grind and polish are relatively perpendicular (100º) to the c-axis and relatively parallel to the interdigitated electrodes. In contrast to Sample 1, the depth of grinding is deeper enough to reach the interdigitation as the indication of such junction structure can be seen in the optical image as a periodic light stripes in Figure 4.6.

After the second stage microindentation (total of 22 indents), the sample was connected to a power supply under an optical microscopy as Figure 4.6 illustrates:

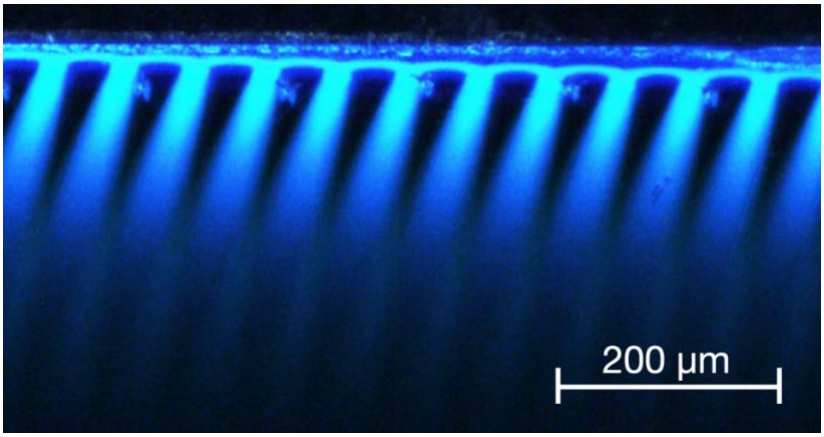

Figure 4.6: Optical image of sample 2 after stage two microindentation with light visible from the microindentation along with the light stripes indicating the photon emission at the junction area.

A clear difference in the optical image of Sample 2 compared to Sample 1 are those periodic light strips which are the result of radiative carrier recombination at the interdigitated junction. The reason why this can be observed is Sample 2 had an extra 10 degree tilted angle and was ground deeper during the sample preparation along with the transparance of the SiC material itself.

The intensity difference between Sample 1 and 2 from the indent in the optical image may be due to image contrast.

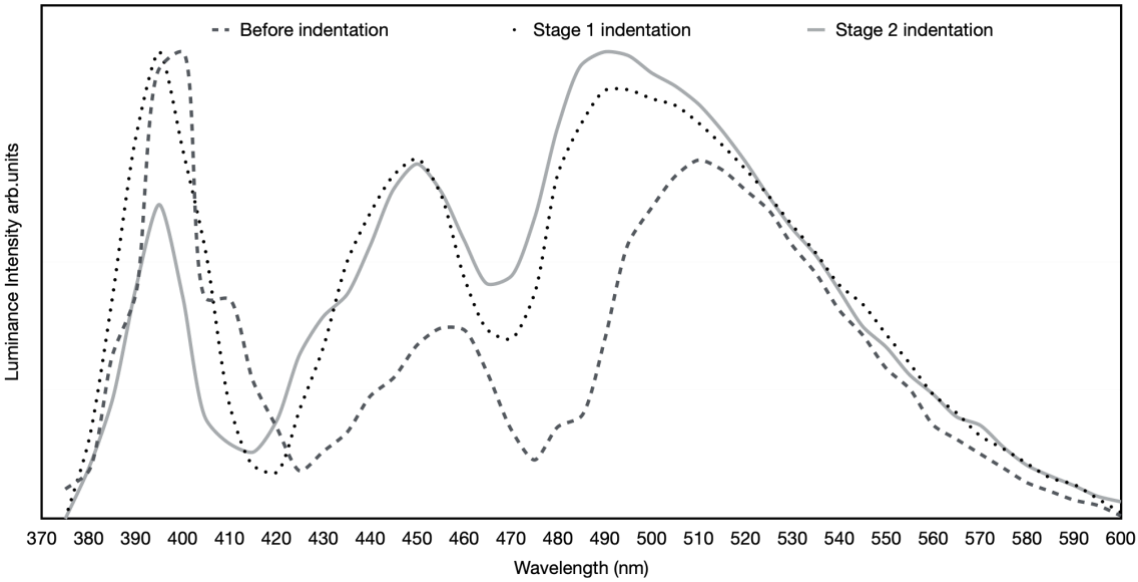

Figure 4.7: Spectrum of sample 2 before and after each indentation stages

Samilar to Sample 1 EL spectra, a 390 nm phonon assisted band to band recombination along with the 445 nm peak and a broadened green peak emission are shown as Figure 4.7.

4.2 Analysis

Spectrum analysis

In addition to the broad green emission, the origin of this new peak centered at 445 nm is also not yet found from the literature review. One theory is that it could be a 4SSFs, quadruple Shockley stacking faults that emits photons at 455 to 460 nm [41]. The emission peak from the 4SSFs, however, does not completely match this observation of 445 nm.

Also, radiative recombination over the area with stacking faults dominates the overall recombination, as will be discussed in Chapter 5, this 445 nm peak is strong yet not the strongest among all three peaks existing in the spectra. Therefore, further analysis is required to understand the mechanism behind this peak.

One more thing to notice is the intensity and tendency of all three peaks under different condtions are different from Sample 1 to Sample 2. Therefore, EL spectra of Sample 1 and 2 are normalized at 390 nm as shown in Figure 4.8 and 4.9.

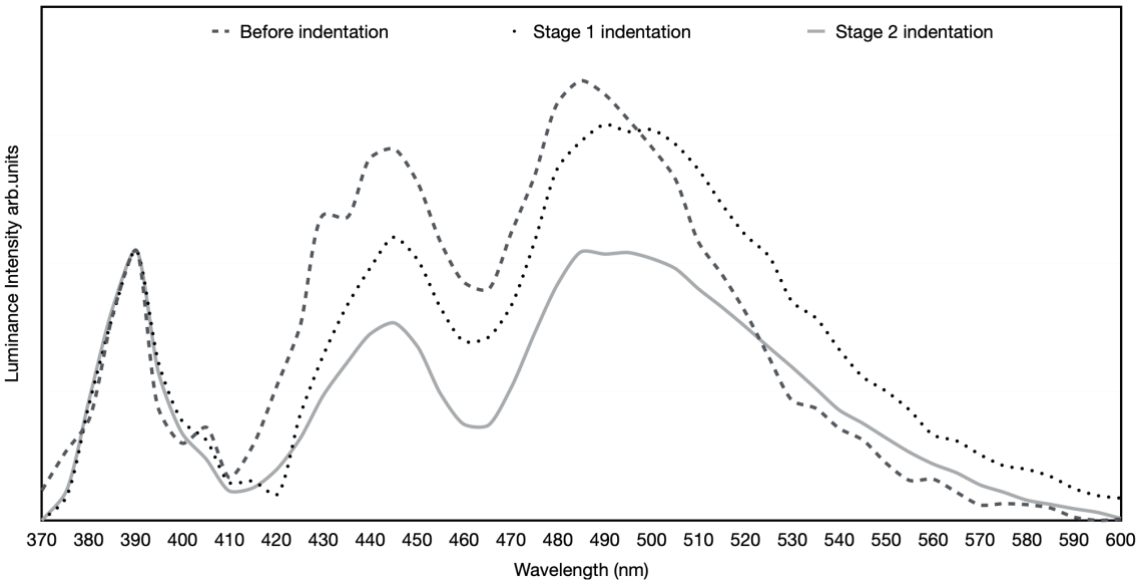

Figure 4.8: Spectrum of sample 1 normalized at 390nm peak

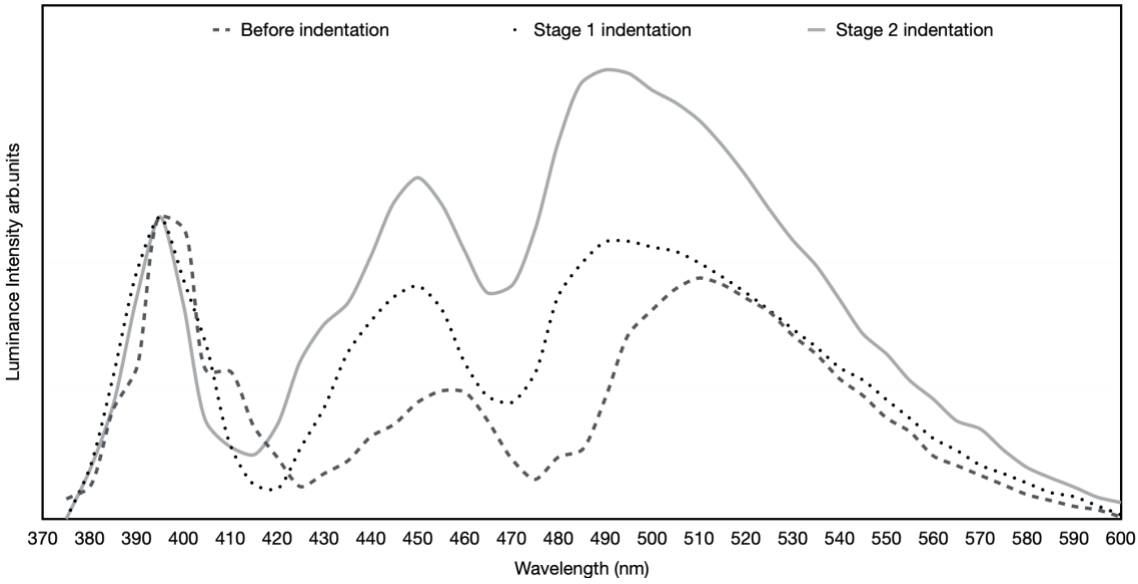

Figure 4.9: Spectrum of sample 2 normalized at 390nm peak

In general, material undergoes plastic deformation when temperature is above the brittle to ductile transition temperature [69]. In the case of 4H-SiC, this temperature would be 1000 to 1200 ºC [70]. In this experiment, samples were tested at room temperature, thus only a limited plastic deformation may occur under microindentation [69].

Excluding the limited plastic deformation, SiC at the surface is more likely to crack during indentation. This is similar to the case of anodic etching, where defects such as dangling bonds and vacancies are expected. Based on the observation from the EL spectra, the broadening of the green emission both occurred in Sample 1 and 2 after indentation. The change of intensity, however, is rather the opposite. Since Sample 2 was ground with a 10º

extra angle, part of the junction has a direct contact to the indented area which may allow carriers to diffuse and recombine over the mechanically generated surface recombination center. Where, on the other hand, for Sample 1, because the indent did not penetrate deep, light exited from the indents adds to the band to band emission. The indentation was probably more like a window for light to exit than a recombination center. But the reason behind the distinction on sample spectra could also simply be the result from the difference of EL response to the carrier injection between each sample. Especially those BJT samples were not designed for light emitting purpose.

IV analysis

IV characterization of Sample 2 is shown in Figure 4.10 and 4.11 under stage 1 indentation.

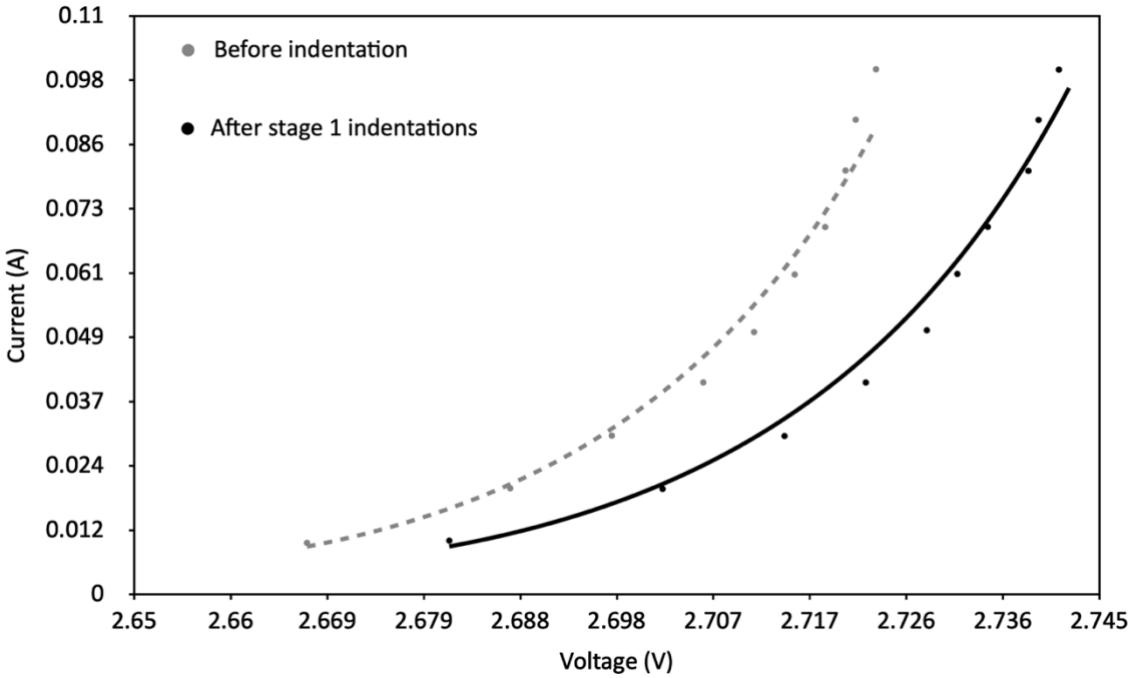

Figure 4.10: IV of sample 2 before and after first stage indentation

Notice that temperature starts to affect the IV characteristic at high current due to phonon assistance, shown as a steeper slope in Figure 4.10.

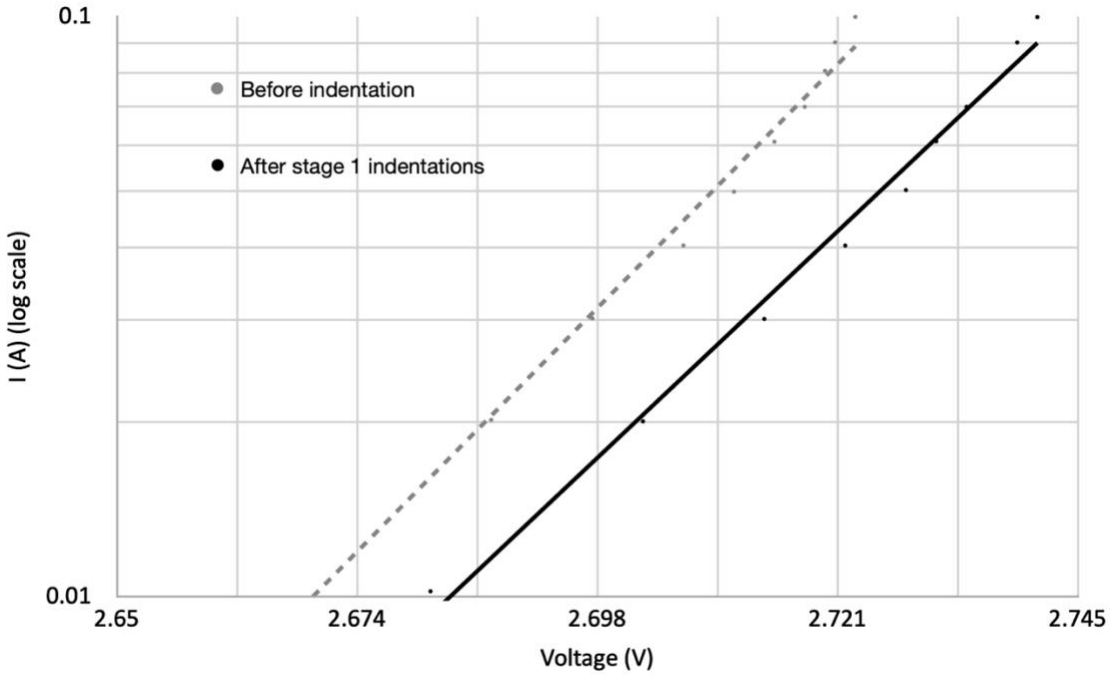

Figure 4.11: IV of sample 2 before and after first stage indentation in semi-log scale

The IV characterization of Sample 2 before and after indentation is shown in both scales to indicate a change of power consumption due to the indentation. Higher power consumption is expected due to the defects that are newly generated. However, the ideality factor *n* seems not much affected by the process as the shape of the slope did not vary significantly.

Chapter 5

Effect of Stacking Faults on Spectrum of 4H-SiC

5.1 Effects of Etching on Spectrum of 4H-SiC with Stacking Faults

Sample a:

EL spectra of Sample 4 from the Chapter 3 were observed with the characteristic of stacking faults formation. The data of Sample a (4 from the Chapter 3) is shown in Table 5.1.

Sample number	Treatment	Ideality factor	Major recombination in theory
Sample a	Intermediate surface exposure	4.373 (before) 4.711(after)	Stacking faults

Table 5.1: Sample preparation and major recombination mechanisms of sample a

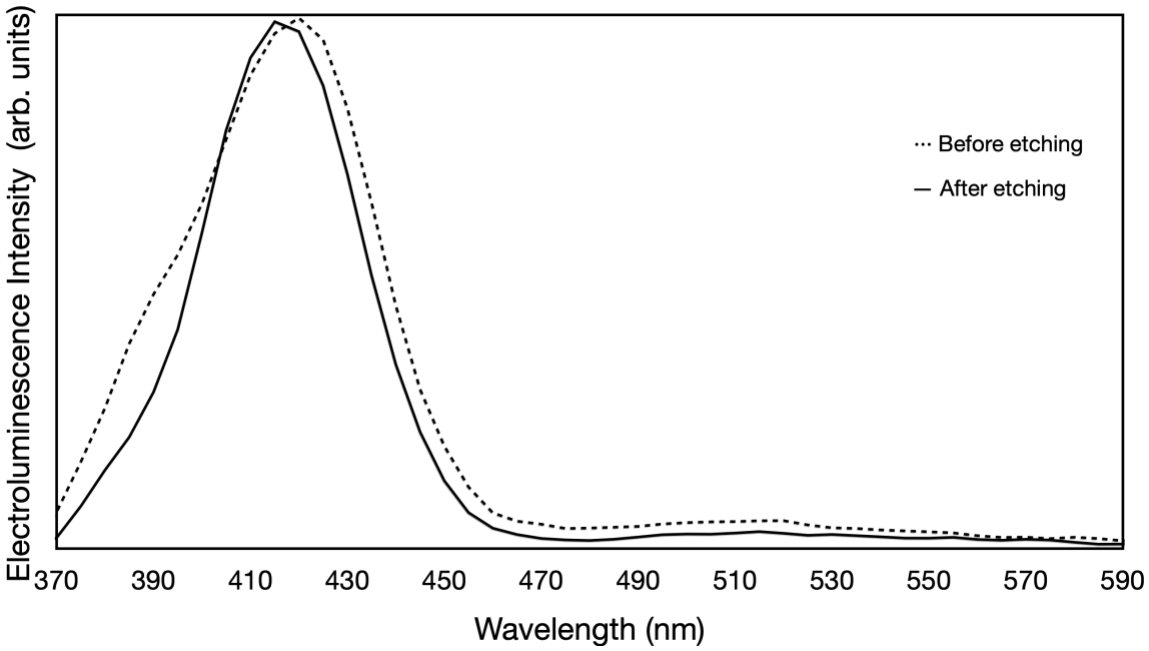

Figure 5.1: Spectrum of sample a before and after etching

Depending on the structure of the stacking fault, carriers recombine at a set of specific energies as discussed in Chapter 2, which gives photon emission at different wavelength as shown in Table 2.2.

Different from all other samples in Chapter 3, the Sample a EL spectra shows a dominant peak at 420 nm which is believed to support the evidence of formation of single Shockley stacking faults or intrinsic Frank stacking faults. Due to the strong confinement of the stacking faults, carriers confined in the structure cannot escape but to recombine at lower energy compared to the band gap of 4H-SiC. The reduced intensity of 390 nm shoulder suggests the band-to-band recombination is no longer observable compared to the 420 nm emission after anodic etching.

IV analysis

The slope of Sample a has a distinction before and after etching with an overall higher ideality factor compared to other samples in Chapter 3. The increased power consumption based on the observation from Figure 5.2 indicates the instability and device degradation induced by the stacking faults along with anodic etching. Also as mentioned in Chapter 2, a higher ideality factor was discovered from this sample with the value of n more than 4, which has a similar IV characteristic to those compound semiconductors that uses quantum wells for photon emission at selective wavelength [63].

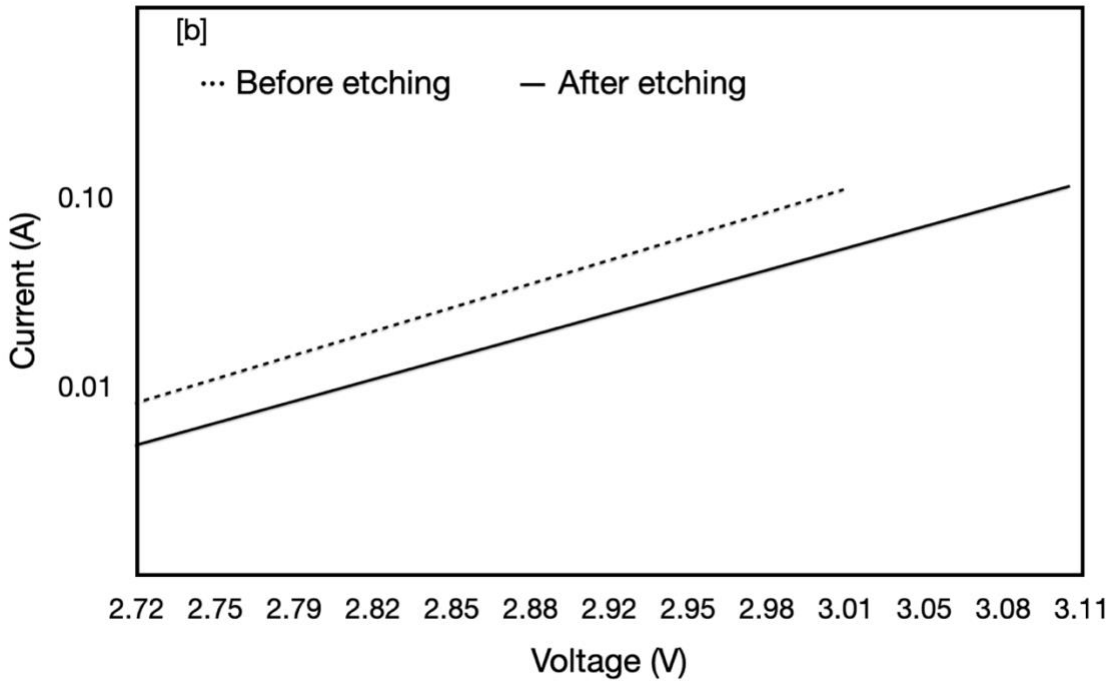

Figure 5.2: IV of sample a before and after etching in semi-log scale

5.2 Effects of Microindentation on Spectrum of 4H-SiC with Stacking Faults

Sample b:

Sample b is same as Sample 3 in Chapter 4 which shows a strong emission at 420nm that corelate to SFs formation.

The treatment of Sample b (3 in Chapter 4) is shown in Table 5.2.

Sample Number	Exposed die edge	θ	Load (Gram-Force)	Number of Stage 1 Indentation	Total Number After Stage 2 Indentation
Sample b	// to interdigitations	90	200	11	22

Table 5.2: Sample preparation for microindentation for sample b

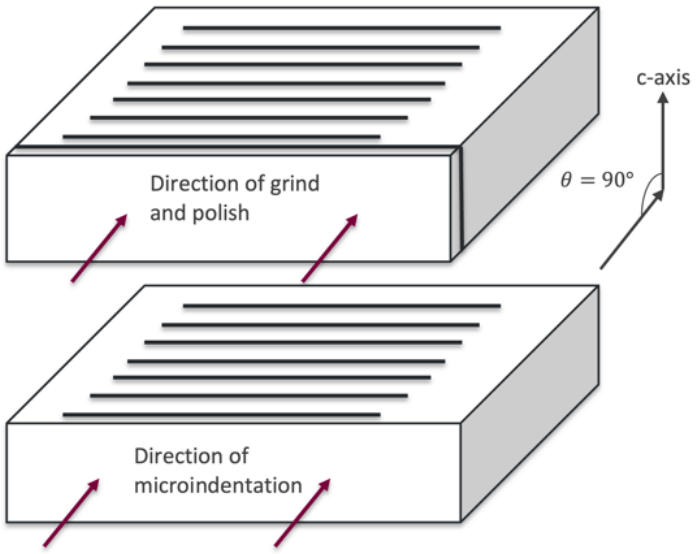

Figure 5.3: Structure of the sample b showing the direction of polish and grind with respect to the direction of microindentation.

Figure 5.3 above shows the inside look of front polishing. The direction of grind and polish are perpendicular to the c-axis and the interdigitated electrodes. Compared to Sample 2 in Chapter 4, the structure of the interdigitation cannot be observed due to this viewing angle.

Notice the change of polishing and grinding direction does not change the material property; thus, it is not the cause of the 420 nm peak shown later in Figure 5.5.

After the second stage microindentation (total of 22 indents), the sample was connected to a power supply under an optical microscopy as Figure 5.4 illustrates:

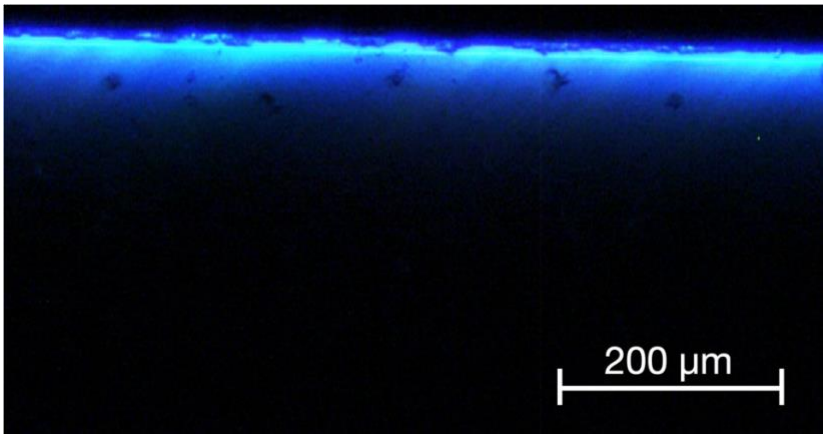

Figure 5.4: Optical image of sample b after stage two microindentation

As distinct from Sample 1 and 2, no clear light can be seen from the indents. In the real image shown in the Appendix, the colour difference between each sample can be observed clearly. Sample b has a mixed light output as part of the non-faulted region emits light that are very close to what were observed from other as-received samples.

Also in Appendix, real image of Sample b under different current flow: 0.05 A, 0.13 A and 0.20 A are shown.

Spectrum analysis

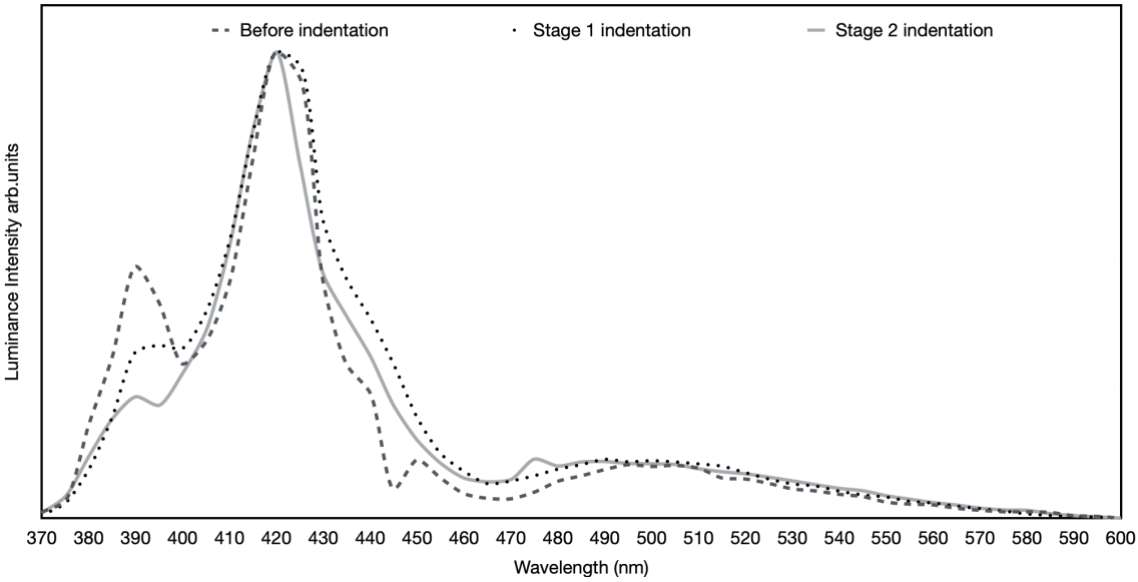

Figure 5.5: Spectrum of sample b before and after each indentation stages

As opposed to all other sampeles in Chapter 4, a relatively weak 390 nm phonon assisted band to band recombination along with a dominatnt 420 nm peak are present in the EL spectra of Sample b as shown in Figure 5.5. The broadened green emission is hardly visible compare to the other two peaks. This 420 nm peak also indicates a formation of single Shockley SFs or instrinc Frank SFs inside the material as discussed in previous chapters.

To better compare the influence of microindentation to the Sample b, EL spectra are normalized at 390 nm as shown in Figure 5.6.

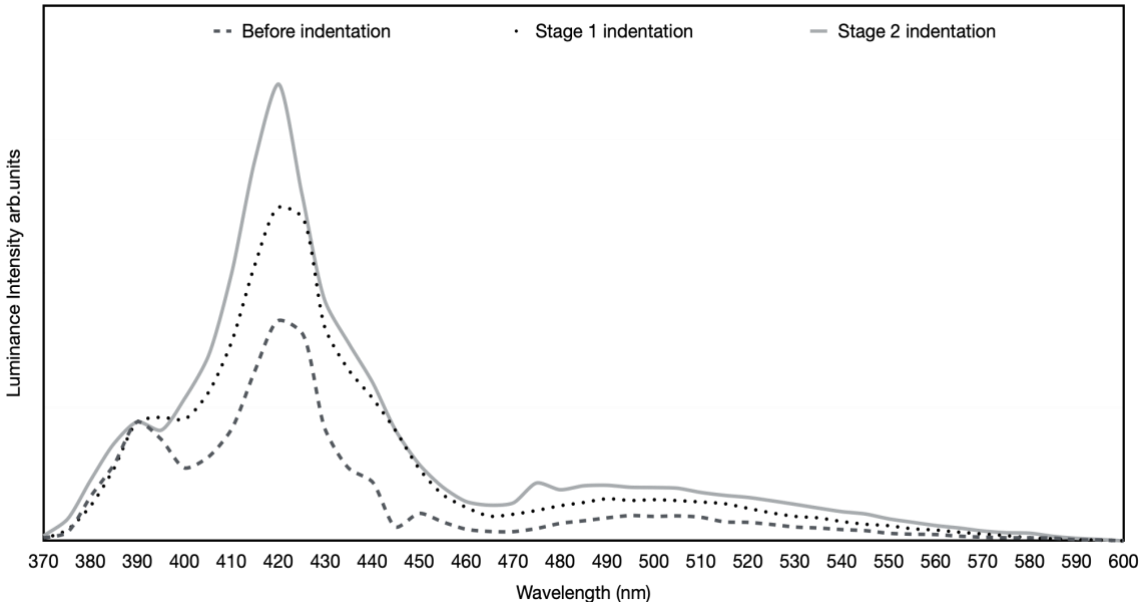

Figure 5.6: Spectrum of sample b normalized at 390nm peak

A relative increase of 420 nm emission compared to the 390 nm emission can be seen in Figure 5.6. Nucleation of dislocations and stacking faults extension were previously observed from a 6H-SiC [62] under nanoindentation at room temperature. This may be the result of extension of SFs due to microindentation induced dislocation glide or a reduction of band to band recombination as more defects are introduced into the system.

IV analysis

As the major recombination event in Sample b is different form the non-faulted samples, the IV characteristic are also tested to support the statement of the negative impact of stacking fault to the device stability. Figure 5.7 and 5.8 shows the IV characteristic of Sample b in two scales.

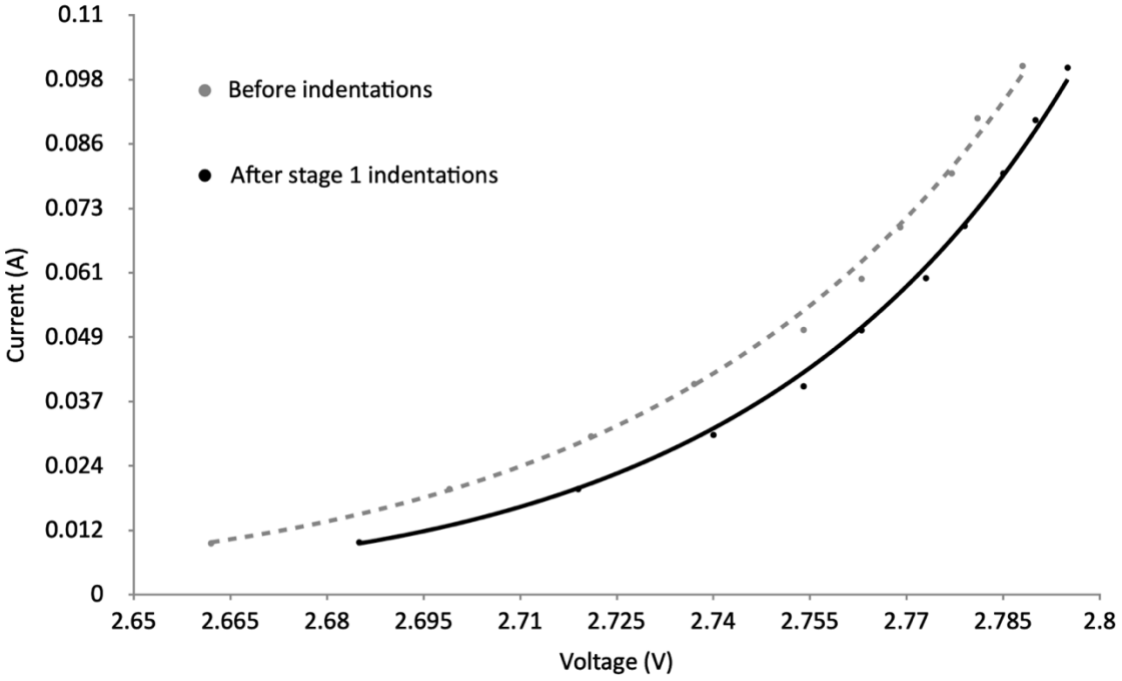

Figure 5.7: IV of sample b before and after first stage indentation

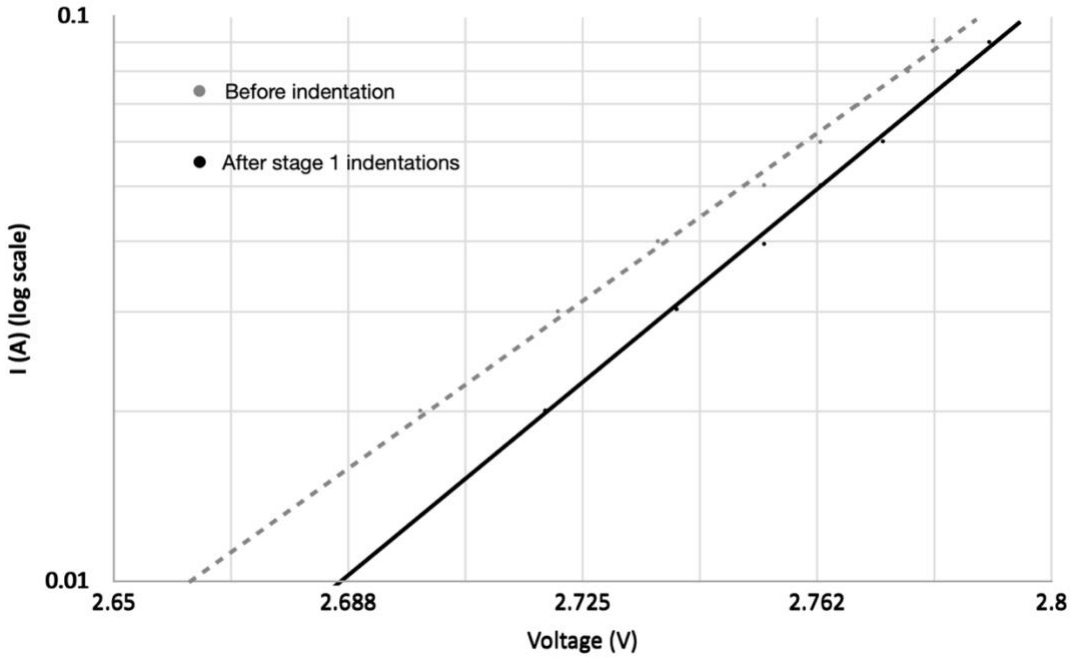

Figure 5.8: IV of sample b before and after first stage indentation in semi-log scale

Before indentation, the ideality factor *n* of Sample 3 was 2.12. After indentation, however, the voltage reading started to fluctuate, especially after Stage 2 indentation. The image shown in Figures 5.7 and 5.8 were taken when readings were stable. This shows how much damage stacking faults with a combined influence from the external stress could do to device stability. Also seen from Figure 5.7, the high current seems did not influence the IV of Sample b as was expected on those samples without SFs as seen in Figure 4.10.

Chapter 6

Conclusion

In this work, the EL and IV results of 4H-SiC BJT samples were tested to analyse the effect of various defects on the spectra. Despite the constantly observed phonon assisted band to band recombination at 390 nm, other peaks centered at 500 nm and 445 nm were also detected. Although the mechanism behind those emission peaks is not fully determined, some speculations were made. Stacking faults observed during testing shows a negative impact to the device stability. The defects generated by anodic etching and microindentation broadened the green emission due to the surface defects that also favours stacking faults as the band to band recombination is further suppressed.

Chapter 7

Future work

Some other techniques like etch pit, TEM and X-ray analysis are also powerful to characterize extended defects. Within particular, HRTEM that can locate and show stacking faults at the atomic level. The future work may include the use of these techniques to characterize defects and identify the origin of 445 and 500 nm peaks.

In addition to that, point defects potentially generated during fabrication by ion implantation and doping were not covered and the EL spectra did not include the range of emission wavelengths associated with some of the point defects, as many of them are closer to the infra-red region. Those point defects are also worth to study. In particular, colour centers inside silicon carbide have a great potential on future applications such as quantum information processes and single photon emitters.

Appendix A

Microhardness tester

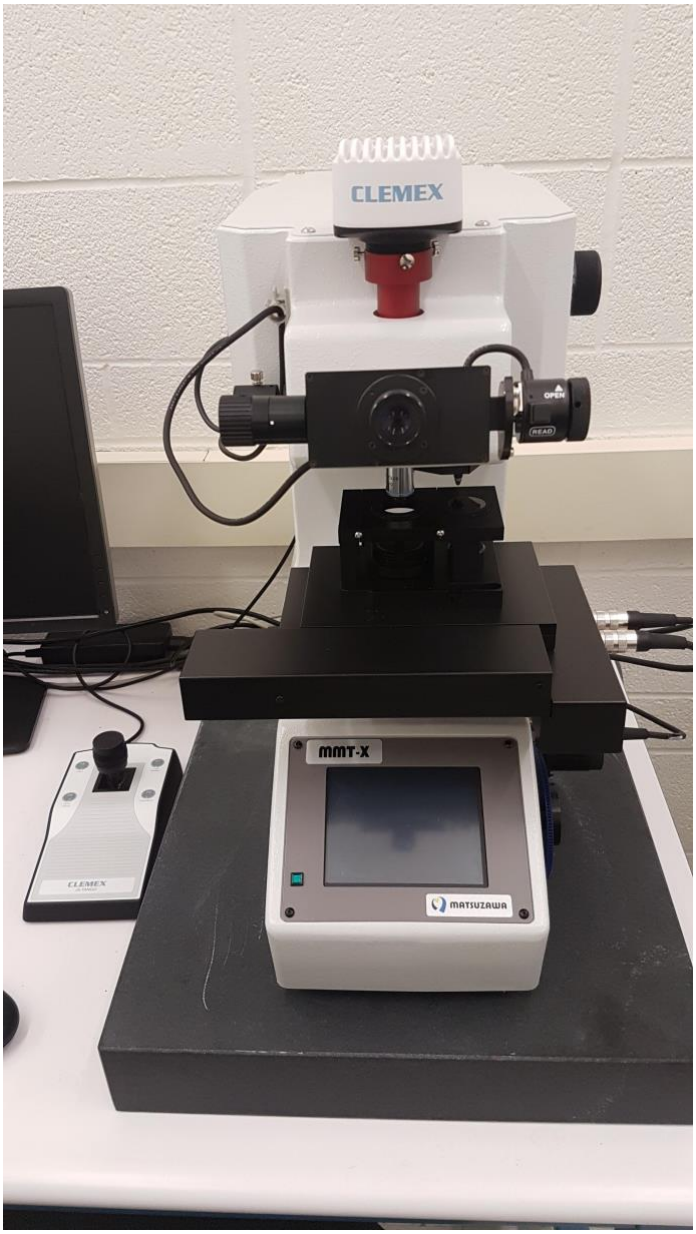

Appendix B

Polishing direction:

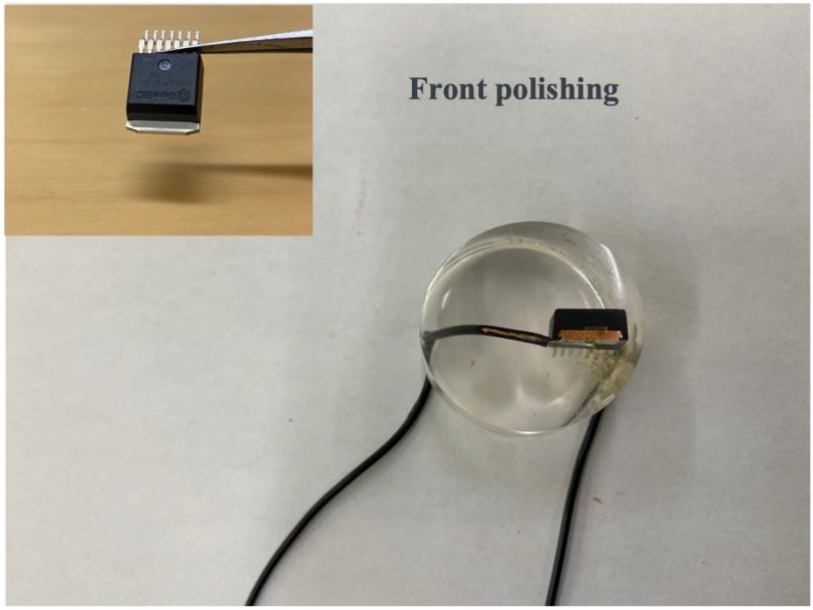

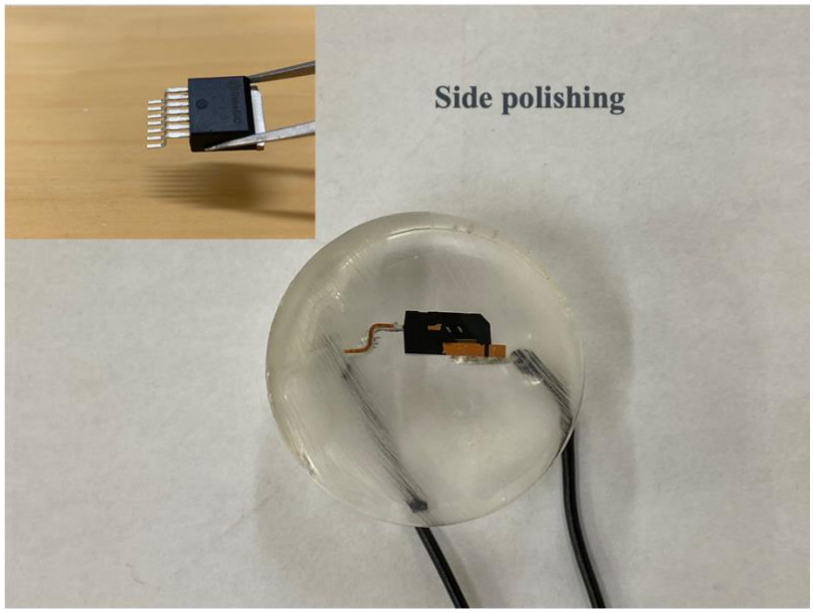

Real images:

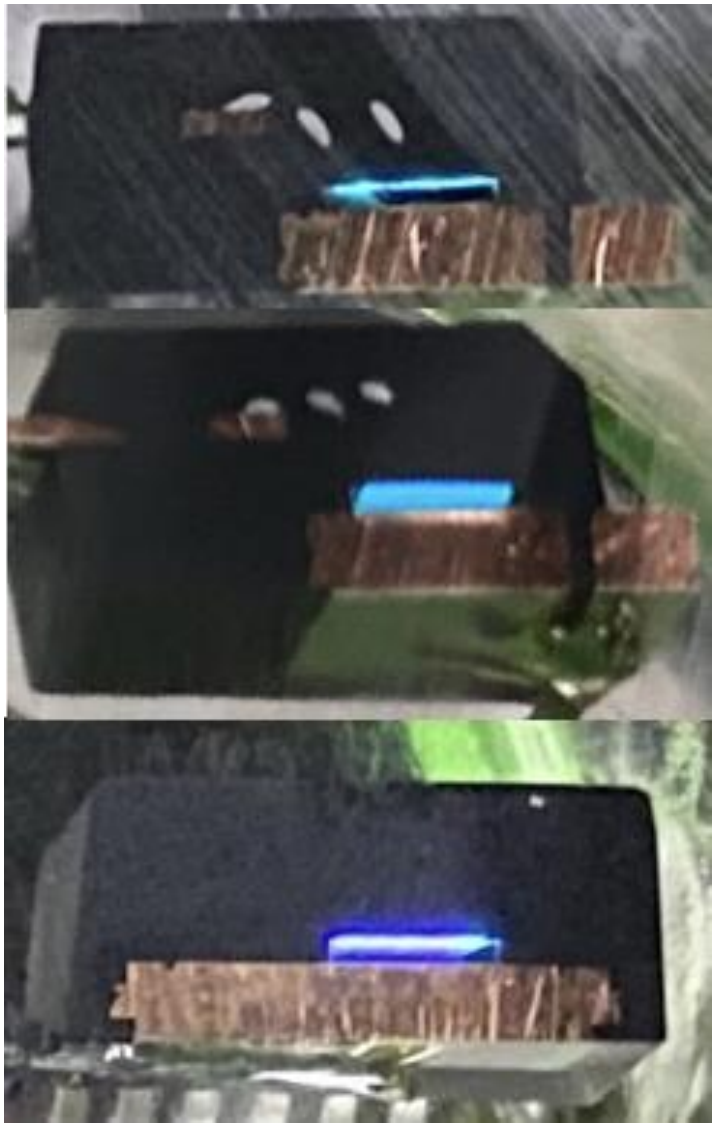

Real image of sample 1,2,3 (b in Chapter 5)

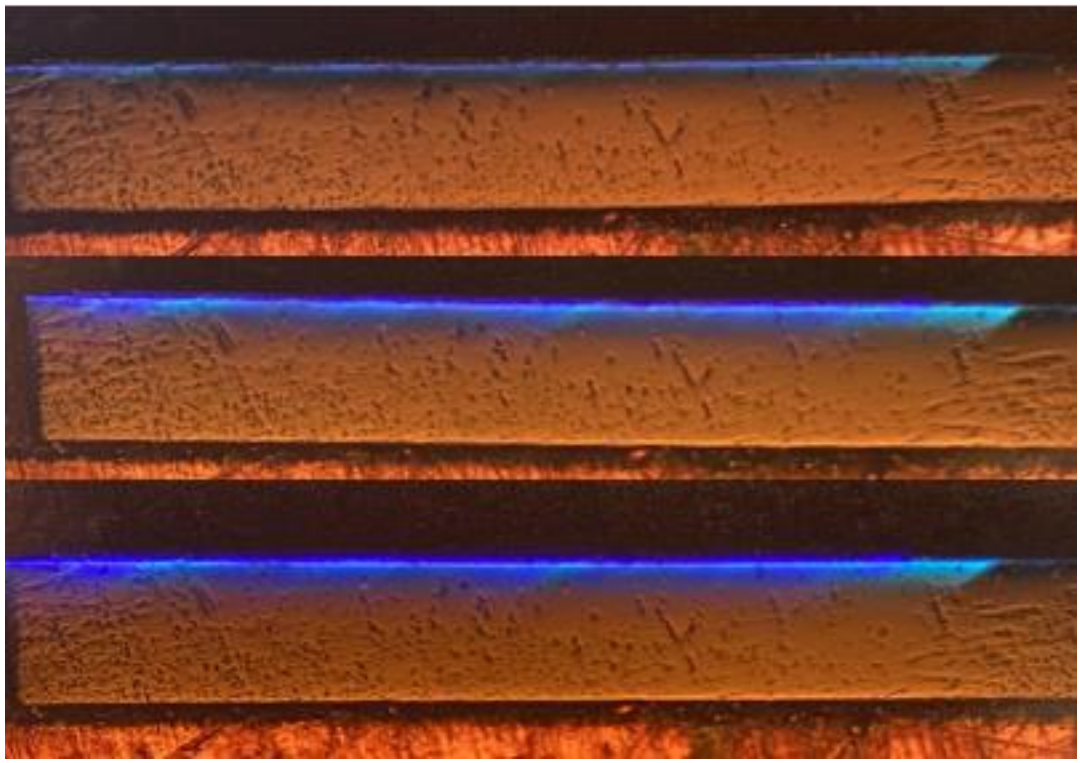

Image of sample 3 (b in Chapter 5) under different flow of current

Bibliography

[1] Casady, J., & Johnson, R. (1996). Status of silicon carbide (SiC) as a wide-bandgap semiconductor for high-temperature applications: A review. *Solid-State Electronics*, ***39***(10), 1409-1422. doi: 10.1016/0038-1101(96)00045-7

[2] *Neudeck, P.G. (2006). Silicon Carbide Technology.*

[3] Okumura, H., 2006. Present Status and Future Prospect of Widegap Semiconductor High-Power Devices. *Japanese Journal of Applied Physics*, **45**(10A), pp.7565-7586.

[4] Kaji, N., Suda, J., & Kimoto, T. (2015). Temperature dependence of forward characteristics for ultrahigh-voltage SiC p–i–n diodes with a long carrier lifetime. *Japanese Journal Of Applied Physics*, ***54***(9), 098004. doi: 10.7567/jjap.54.098004

[5] Bhatnagar, M., & Baliga, B. (1993). Comparison of 6H-SiC, 3C-SiC, and Si for power devices. *IEEE Transactions On Electron Devices*, ***40***(3), 645-655. doi: 10.1109/16.199372

[6] Cooper, J., & Agarwal, A. (2002). SiC power-switching devices-the second electronics revolution?. *Proceedings Of The IEEE*, ***90***(6), 956-968. doi: 10.1109/jproc.2002.1021561

[7] Harada, S., Kobayashi, Y., Ariyoshi, K., Kojima, T., Senzaki, J., Tanaka, Y., & Okumura, H. (2016). 3.3-kV-Class 4H-SiC MeV-Implanted UMOSFET With Reduced Gate Oxide Field. *IEEE Electron Device Letters*, ***37***(3), 314-316. doi: 10.1109/led.2016.2520464

[8] Imaizumi, M., & Miura, N. (2015). Characteristics of 600, 1200, and 3300 V Planar SiC-MOSFETs for Energy Conversion Applications. *IEEE Transactions On Electron Devices*, ***62***(2), 390-395. doi: 10.1109/ted.2014.2358581

[9] Kimoto, T., Yamada, K., Niwa, H., & Suda, J. (2016). Promise and Challenges of High-Voltage SiC Bipolar Power Devices. *Energies*, ***9***(11), 908. doi: 10.3390/en9110908

[10] Fuchs, F., Soltamov, V., Väth, S., Baranov, P., Mokhov, E., Astakhov, G., & Dyakonov, V. (2013). Silicon carbide light-emitting diode as a prospective room temperature source for single photons. *Scientific Reports*, ***3***(1). doi: 10.1038/srep01637

[11] Nevin, W., Yamagishi, H., Yamaguchi, M., & Tawada, Y. (1994). Emission of blue light from hydrogenated amorphous silicon carbide. *Nature*, ***368***(6471), 529-531. doi: 10.1038/368529a0

[12] Lin, S. (2012). Light-Emitting Two-Dimensional Ultrathin Silicon Carbide. *The Journal Of Physical Chemistry C*, ***116***(6), 3951-3955. doi: 10.1021/jp210536m

[13] Zheludev, N. (2007). The life and times of the LED — a 100-year history. *Nature Photonics*, ***1***(4), 189-192. doi: 10.1038/nphoton.2007.34

[14] Caldwell, J., Giles, A., Lepage, D., Carrier, D., Moumanis, K., & Hull, B. et al. (2013). Experimental evidence for mobile luminescence center mobility on partial dislocations in 4H-SiC using hyperspectral electroluminescence imaging. *Applied Physics Letters*, ***102***(24), 242109. doi: 10.1063/1.4810909

[15] Skowronski, M., & Ha, S. (2006). Degradation of hexagonal silicon-carbide-based bipolar devices. *Journal Of Applied Physics*, ***99***(1), 011101. doi: 10.1063/1.2159578

[16] Kimoto, T. (2015). Material science and device physics in SiC technology for high-voltage power devices. *Japanese Journal Of Applied Physics*, ***54***(4), 040103. doi: 10.7567/jjap.54.040103

[17] Lee, S. (2009). Silicon carbide defects and luminescence centers in current heated 6H-SiC. *Semiconductor Physics, Quantum Electronics And Optoelectronics*, ***13***(1), 024-029. doi: 10.15407/spqeo13.01.024

[18] Kimoto, T., & Cooper, J. (2014). *Fundamentals of silicon carbide technology*. Singapore: John Wiley & Sons Singapore Pte. Ltd.

[19] Wang, M., Zhu, F., Xu, Y., & Liu, S. (2018). Investigation of Nanocutting Characteristics of Off-Axis 4H-SiC Substrate by Molecular Dynamics. *Applied Sciences*, ***8***(12), 2380. doi: 10.3390/app8122380

[20] Cooper, J., Melloch, M., Singh, R., Agarwal, A., & Palmour, J. (2002). Status and prospects for SiC power MOSFETs. *IEEE Transactions On Electron Devices*, ***49***(4), 658-664. doi: 10.1109/16.992876

[21] Friedrichs, P. (2008). Silicon carbide power-device products - Status and upcoming challenges with a special attention to traditional, nonmilitary industrial applications. *Physica Status Solidi (B)*, ***245***(7), 1232-1238. doi: 10.1002/pssb.200743478

[22] Yoo, W., & Matsunami, H. (1991). Solid-State Phase Transformation in Cubic Silicon Carbide. *Japanese Journal Of Applied Physics*, ***30***(Part 1, No. 3), 545-553. doi: 10.1143/jjap.30.545

[23] Iwata, H., Lindefelt, U., Öberg, S., & Briddon, P. (2003). Stacking faults in silicon carbide. *Physica B: Condensed Matter*, *340-342*, 165-170. doi: 10.1016/j.physb.2003.09.045

[24] Ivanov, Ivan & Lindefelt, U. & Henry, A. & Kordina, Olof & Hallin, Christophe & Aroyo, M. & Egilsson, T. & Janzén, E.. (1998). Phonon replicas at the M point in 4H-SiC: A theoretical and experimental study. Phys. Rev. B. 58. 13634. 10.1103/PhysRevB.58.13634.

[25] Kimoto, T., Hiyoshi, T., Hayashi, T., & Suda, J. (2010). Impacts of recombination at the surface and in the substrate on carrier lifetimes of n-type 4H–SiC epilayers. *Journal Of Applied Physics*, ***108***(8), 083721. doi: 10.1063/1.3498818

[26] Miyazawa, T., Ito, M., & Tsuchida, H. (2010). Evaluation of long carrier lifetimes in thick 4H silicon carbide epitaxial layers. *Applied Physics Letters*, ***97***(20), 202106. doi: 10.1063/1.3517487

[27] Marshak, A., & Assaf, D. (1973). A generalized Einstein relation for semiconductors. *Solid-State Electronics*, ***16***(6), 675-679. doi: 10.1016/0038-1101(73)90110-x

[28] Kimoto, T. (2016). Bulk and epitaxial growth of silicon carbide. *Progress In Crystal Growth And Characterization Of Materials*, ***62***(2), 329-351. doi: 10.1016/j.pcrysgrow.2016.04.018

[29] Blevins, J. (2020). Development of a World Class Silicon Carbide Substrate Manufacturing Capability. *IEEE Transactions On Semiconductor Manufacturing*, ***33***(4), 539-545. doi: 10.1109/tsm.2020.3028036

[30] Meli, A., Muoio, A., Trotta, A., Meda, L., Parisi, M., & La Via, F. (2021). Epitaxial Growth and Characterization of 4H-SiC for Neutron Detection Applications. *Materials*, ***14***(4), 976. doi: 10.3390/ma14040976

[31] Mahadik, N., Stahlbush, R., Qadri, S., Glembocki, O., Alexson, D., & Hobart, K. et al. (2011). Structure and Morphology of Inclusions in 4° Offcut 4H-SiC Epitaxial Layers. *Journal Of Electronic Materials*, ***40***(4), 413-418. doi: 10.1007/s11664-011-1570-8

[32] Ha, S., Mieszkowski, P., Skowronski, M., & Rowland, L. (2002). Dislocation conversion in 4H silicon carbide epitaxy. *Journal Of Crystal Growth*, ***244***(3-4), 257-266. doi: 10.1016/s0022-0248(02)01706-2

[33] Mahadik, N., Stahlbush, R., Ancona, M., Imhoff, E., Hobart, K., & Myers-Ward, R. et al. (2012). Observation of stacking faults from basal plane dislocations in highly doped 4H-SiC epilayers. *Applied Physics Letters*, ***100***(4), 042102. doi: 10.1063/1.3679609

[34] Yazdanfar, M., Pedersen, H., Kordina, O., & Janzén, E. (2014). Effect of Process Parameters on Dislocation Density in Thick 4H-SiC Epitaxial Layers Grown by Chloride-Based CVD on 4° Off-Axis Substrates. *Materials Science Forum*, *778-780*, 159-162. doi: 10.4028/www.scientific.net/msf.778-780.159

[35] Neudeck, P., & Powell, J. (1994). Performance limiting micropipe defects in silicon carbide wafers. *IEEE Electron Device Letters*, ***15***(2), 63-65. doi: 10.1109/55.285372

[36] Steiner, Johannes & Roder, Melissa & Nguyen, Binh Duong & Sandfeld, Stefan & Danilewsky, Andreas & Wellmann, Peter. (2019). Analysis of the Basal Plane Dislocation Density and Thermomechanical Stress during 100 mm PVT Growth of 4H-SiC. Materials. 12. 2207. 10.3390/ma12132207.

[37] Ohtani, N., Katsuno, M., Tsuge, H., Fujimoto, T., Nakabayashi, M., & Yashiro, H. et al. (2006). Propagation behavior of threading dislocations during physical vapor transport growth of silicon carbide (SiC) single crystals. *Journal Of Crystal Growth*, ***286***(1), 55-60. doi: 10.1016/j.jcrysgro.2005.09.030

[38] Bergman, P., Lendenmann, H., Nilsson, P., Lindefelt, U., & Skytt, P. (2001). Crystal Defects as Source of Anomalous Forward Voltage Increase of 4H-SiC Diodes. *Materials Science Forum*, *353-356*, 299-302. doi: 10.4028/www.scientific.net/msf.353-356.299

[39] Agarwal, A., Fatima, H., Haney, S., & Ryu, S. (2007). A New Degradation Mechanism in High-Voltage SiC Power MOSFETs. *IEEE Electron Device Letters*, ***28***(7), 587-589. doi: 10.1109/led.2007.897861

[40] Caldwell, J., Stahlbush, R., Ancona, M., Glembocki, O., & Hobart, K. (2010). On the driving force for recombination-induced stacking fault motion in 4H–SiC. *Journal Of Applied Physics*, ***108***(4), 044503. doi: 10.1063/1.3467793

[41] Feng, G., Suda, J., & Kimoto, T. (2009). Triple Shockley type stacking faults in 4H-SiC epilayers. *Applied Physics Letters*, ***94***(9), 091910. doi: 10.1063/1.3095508

[42] Zhang, Z., Maximenko, S., Shrivastava, A., Sadagopan, P., Gao, Y., & Sudarshan, T. (2006). Propagation of stacking faults from surface damage in SiC PiN diodes. *Applied Physics Letters*, ***88***(6), 062101. doi: 10.1063/1.2172015

[43] Galeckas, A., Linnros, J., & Pirouz, P. (2006). Recombination-Induced Stacking Faults: Evidence for a General Mechanism in Hexagonal SiC. *Physical Review Letters*, ***96***(2). doi: 10.1103/physrevlett.96.025502

[43] Kim, H., Kim, S., Kim, S., Lee, N., Shin, H., & Lee, C. (2020). Relation between work function and structural properties of triangular defects in 4H-SiC epitaxial layer: Kelvin probe force microscopic and spectroscopic analyses. *Nanoscale*, ***12***(15), 8216-8229. doi: 10.1039/c9nr10126h

[44]Iwata, H., Lindefelt, U., Öberg, S., & Briddon, P. (2001). Localized electronic states around stacking faults in silicon carbide. *Physical Review B*, ***65***(3). doi: 10.1103/physrevb.65.033203

[45] Iijima, A., & Kimoto, T. (2019). Electronic energy model for single Shockley stacking fault formation in 4H-SiC crystals. *Journal Of Applied Physics*, ***126***(10), 105703. doi: 10.1063/1.5117350

[46] Sridhara, S., Carlsson, F., Bergman, J., & Janzén, E. (2001). Luminescence from stacking faults in 4H SiC. *Applied Physics Letters*, ***79***(24), 3944-3946. doi: 10.1063/1.1425084

[47] Hong, M., Samant, A., & Pirouz, P. (2000). Stacking Fault Energy of 6H-SiC and 4H-SiC Single Crystals. *Materials Science Forum*, *338-342*, 513-516. doi: 10.4028/www.scientific.net/msf.338-342.513

[48] Tsuchida, H., Kamata, I., & Nagano, M. (2008). Formation of basal plane Frank-type faults in 4H-SiC epitaxial growth. *Journal Of Crystal Growth*, ***310***(4), 757-765. https://doi.org/10.1016/j.jcrysgro.2007.11.156

[49] Hassan, J., Henry, A., McNally, P. and Bergman, J., 2010. Characterization of the carrot defect in 4H-SiC epitaxial layers. *Journal of Crystal Growth*, ***312***(11), pp.1828-1837.

[50] Okada, T., Kimoto, T., Yamai, K., Matsunami, H. and Inoko, F., 2003. Crystallographic defects under device-killing surface faults in a homoepitaxially grown film of SiC. *Materials Science and Engineering: A*, ***361***(1-2), pp.67-74.

[51] Konstantinov, A., Hallin, C., Pécz, B., Kordina, O. and Janzén, E., 1997. The mechanism for cubic SiC formation on off-oriented substrates. *Journal of Crystal Growth*, ***178***(4), pp.495-504.

[52] Okada, T., Kimoto, T., Noda, H., Ebisui, T., Matsunami, H. and Inoko, F., 2002. Correspondence between Surface Morphological Faults and Crystallographic Defects in 4H–SiC Homoepitaxial Film. *Japanese Journal of Applied Physics*, ***41***(Part 1, No. 11A), pp.6320-6326.

[53] Brillson, L., Tumakha, S., Okojie, R., Zhang, M. and Pirouz, P., 2004. Electron-excited luminescence of SiC surfaces and interfaces. *Journal of Physics: Condensed Matter*, ***16***(17), pp.S1733-S1754.

[54] Gulbinas, K,. Grivickas, V., Mahabadi, H., Usman, M. and Hallén, A., 2011. Surface Recombination Investigation in Thin 4H-SiC Layers. *Materials Science*, ***17***(2), pp.119-124.

[55] Cadiz, F., Paget, D., Rowe, A., Berkovits, V., Ulin, V., Arscott, S. and Peytavit, E., 2013. Surface recombination in doped semiconductors: Effect of light excitation power and of surface passivation. *Journal of Applied Physics*, ***114***(10), p.103711.

[56] Konstantinov, A., Henry, A., Harris, C. and Janzén, E., 1995. Photoluminescence studies of porous silicon carbide. *Applied Physics Letters*, ***66***(17), pp.2250-2252.

[57] Lu, W., Tarekegne, A., Ou, Y., Kamiyama, S. and Ou, H., 2019. Temperature-dependent photoluminescence properties of porous fluorescent SiC. *Scientific Reports*, ***9***(1).

[58] Lu, W., Ou, Y., Fiordaliso, E., Iwasa, Y., Jokubavicius, V., & Syväjärvi, M. et al. (2017). White Light Emission from Fluorescent SiC with Porous Surface. *Scientific Reports*, ***7***(1). doi: 10.1038/s41598-017-10771

[59] Feng, G., Suda, J., & Kimoto, T. (2008). Characterization of stacking faults in 4H-SiC epilayers by room-temperature microphotoluminescence mapping. *Applied Physics Letters*, ***92***(22), 221906. doi: 10.1063/1.2937097

[60] Kamata, I., Zhang, X., & Tsuchida, H. (2012). Photoluminescence Imaging and Wavelength Analysis of Basal Plane Frank-Type Defects in 4H-SiC Epilayers. *Materials Science Forum*, *725*, 15-18. doi: 10.4028/www.scientific.net/msf.725.15

[61] Chung, S., Berechman, R., McCartney, M., & Skowronski, M. (2011). Electronic structure analysis of threading screw dislocations in 4H–SiC using electron holography. *Journal Of Applied Physics*, ***109***(3), 034906. doi: 10.1063/1.3544066

[62] Wu, Z., Liu, W., Zhang, L., & Lim, S. (2020). Amorphization and Dislocation Evolution Mechanisms of Single Crystalline 6H-SiC. *SSRN Electronic Journal*. doi: 10.2139/ssrn.3384328

[63] Shah, J., Li, Y., Gessmann, T., & Schubert, E. (2003). Experimental analysis and theoretical model for anomalously high ideality factors (n≫2.0) in AlGaN/GaNp-njunction diodes. *Journal Of Applied Physics*, ***94***(4), 2627-2630. doi: 10.1063/1.1593218

[64] Juillaguet, S., Albrecht, M., Camassel, J., & Chassagne, T. (2007). Cathodoluminescence investigation of stacking faults extension in 4H-SiC. *Physica Status Solidi (A)*, ***204***(7), 2222-2228. doi: 10.1002/pssa.200675469

[65] Yamamoto, H. (2013). Assessment of Stacking Faults in Silicon Carbide Crystals. *Sensors And Materials*, 177. doi: 10.18494/sam.2013.852

[66] Shinagawa, N., Izawa, T., Manabe, M., Yamochi, T., & Ohtani, N. (2020). Populations and propagation behaviors of pure and mixed threading screw dislocations in physical vapor transport grown 4H-SiC crystals investigated using X-ray topography. *Japanese Journal Of Applied Physics*, ***59***(9), 091002. doi: 10.35848/1347-4065/abab46

[67] Ishikawa, Y., Yao, Y., Sato, K., Sugawara, Y., Danno, K., & Suzuki, H. et al. (2011). Detection of Shallow Dislocations on 4H-SiC Substrate by Etching Method. *Acta Physica Polonica A*, ***120***(6A), A-25-A-27. doi: 10.12693/aphyspola.120.a-25

[68] Galeckas, A., Linnros, J., & Pirouz, P. (2002). Recombination-enhanced extension of Stacking Faults in 4H-SiC p-i-n diodes under forward bias *Applied Physics Letters*, ***81***(883). doi: 10.1063/1.1496498.

[69] Demenet, J., Hong, M., & Pirouz, P. (2000). Plastic behavior of 4H-SiC single crystals deformed at low strain rates. *Scripta Materialia*, ***43***(9), 865-870. doi: 10.1016/s1359-6462(00)00495-4

[70] Pirouz, P., Zhang, M., Demenet, J., & Hobgood, H. (2002). Transition from brittleness to ductility in SiC. *Journal Of Physics: Condensed Matter*, ***14***(48), 12929-12945. doi: 10.1088/0953-8984/14/48/335

Publications:

[1] Bawa, S., Zhang, T., Dow, L., Peter, S., & Kitai, A. (2021). Porous SiC electroluminescence from p–i–n junction and a lateral carrier diffusion model. *Journal Of Applied Physics*, ***129***(4), 044501. doi: 10.1063/5.0033243

[2] Zhang, T., & Kitai, A. (2022). Effect of Microindentation on Electroluminescence of SiC P-I-N Junctions. *Materials*, ***15***(2), 534. doi: 10.3390/ma15020534